doi:10.26443/seismica.v3i1.1102

SEISMICA

Neotectonic Mapping of Puerto Rico

Jessica A. Thompson Jobe * [1], **Richard Briggs** [1], **K. Stephen Hughes** [2], **James Joyce** [2], **Ryan Gold** [1], **Shannon Mahan** [3], **Harrison Gray** [3], **Laura Strickland** [3]

[1]U.S. Geological Survey, Geologic Hazard Science Center, Golden, CO, USA, [2]Department of Geology, University of Puerto Rico Mayagüez, Mayagüez, Puerto Rico, USA, [3]U.S. Geological Survey, Geoscience and Environmental Change Science Center, Denver, CO, USA

Author contributions: *Conceptualization:* J. Thompson Jobe, R. Briggs. *Data Curation:* J. Thompson Jobe, S. Mahan, H. Gray, L. Strickland. *Formal Analysis:* J. Thompson Jobe, R. Briggs, K. S. Hughes, J. Joyce, R. Gold, S. Mahan, H. Gray, L. Strickland. *Investigation:* J. Thompson Jobe, R. Briggs, K. S. Hughes, J. Joyce, R. Gold, S. Mahan, H. Gray, L. Strickland. *Writing - original draft:* J. Thompson Jobe. *Writing - Review & Editing:* J. Thompson Jobe, R. Briggs, K. S. Hughes, J. Joyce, R. Gold, S. Mahan, H. Gray, L. Strickland.

Abstract Puerto Rico is part of the Puerto Rico-Virgin Islands microplate, along the Caribbean–North American plate boundary between the Puerto Rico trench subduction zone and the Muertos Trough incipient subduction zone. Despite recent seismicity and geodetically constrained deformation of ~3 mm/yr of left-lateral shear across the island, Quaternary fault locations remain largely uncertain. Preservation of recent faulting in the landscape is masked by distributed faulting, high weathering rates of the tropical climate, steep topography, widespread landsliding, and extensive agriculture, deforestation, and urbanization throughout the island. We present an updated active fault map of Puerto Rico, created through neotectonic mapping using historical aerial imagery from the 1930s-60s and <1-m lidar topography, integrated with field observations, to create an updated active fault map of Puerto Rico. We focus on faults that offset younger geomorphic surfaces, with ages estimated by geologic mapping, optically stimulated luminescence (OSL) and radiocarbon dating, and morphologic interpretations. We present new evidence for Quaternary activity on seven faults, including the South Lajas, Salinas, Punta Montalva, Great Southern Puerto Rico, Cerro Goden, Parguera, and San Marcos faults. We find that active faulting occurs preferentially near the southern and western coasts and in part spatially coincides with preexisting bedrock faults, possibly reflecting reactivation of some older faults in the modern strain field.

Non-technical summary Puerto Rico experiences moderate to large earthquakes, but the faults that host these earthquakes remain largely unknown. Using high-resolution topographic data of the ground surface from 2019 and historical aerial imagery from the 1930-1960s, we identified and mapped features that indicate possible surface-rupturing earthquakes in the last 10,000 years. These features are located along the southern and western coasts of Puerto Rico. We document seven onshore faults. We also describe an exposure of one of the faults in a road cut at the southern side of the Lajas Valley, with the ages of the sediments indicating that the most recent surface-rupturing earthquake occurred between four to five thousand years ago. The identification of these new faults provides a foundation for an updated active fault map of Puerto Rico and could improve seismic hazard models in the region.

Production Editor:
Gareth Funning
Handling Editor:
Randolph Williams
Copy & Layout Editor:
Anant Hariharan

Received:
September 11, 2023
Accepted:
February 7, 2024
Published:
September 13, 2024

1 Introduction

Puerto Rico is located in a tectonically active region in the northeastern Caribbean, situated on a microplate between the Puerto Rico subduction zone and the Muertos Trough (Figure 1A). Although geodetic data indicate that strain rates across the microplate are low (<1-3 mm/yr, Jansma et al., 2000; Jansma and Mattioli, 2005), the region has experienced several moderate to large earthquakes, including the 1670 A.D. magnitude (M) 6.5–7 (Pacheco and Sykes, 1992; McCann et al., 2010), 1918 M 7.1–7.3 Mona Passage (Reid and Taber, 1919; ten Brink et al., 2023), and most recently, the 2019-ongoing Southwest Puerto Rico seismic sequence (e.g., Vičič et al., 2022). None of these earthquakes ruptured onshore faults, but the presence of fault scarps with dated Holocene surface ruptures (Prentice and Mann, 2005; Piety et al., 2018) demonstrates that onshore fault rupture has happened in the past. Yet to date, no Quaternary fault map of Puerto Rico exists that incorporates interpretations from new high-resolution lidar-derived topography, partly because of the thick vegetation and steep relief present over most of the island that masks signatures of active faulting in the landscape.

Newly available island-wide high-resolution (<1 m) bare-earth lidar-derived digital elevation models (DEMs), available since 2019, allow an unprecedented visualization of the ground surface to document surficial fault expression. In this study, we analyzed the high-resolution topographic data, existing geologic maps, and historical aerial imagery to document evidence of Quaternary fault activity across the island. We mapped faults that clearly deform Quaternary deposits, as classified on existing geologic maps, or through new geomorphic interpretation of the lidar-derived

*Corresponding author: jjobe@usgs.gov

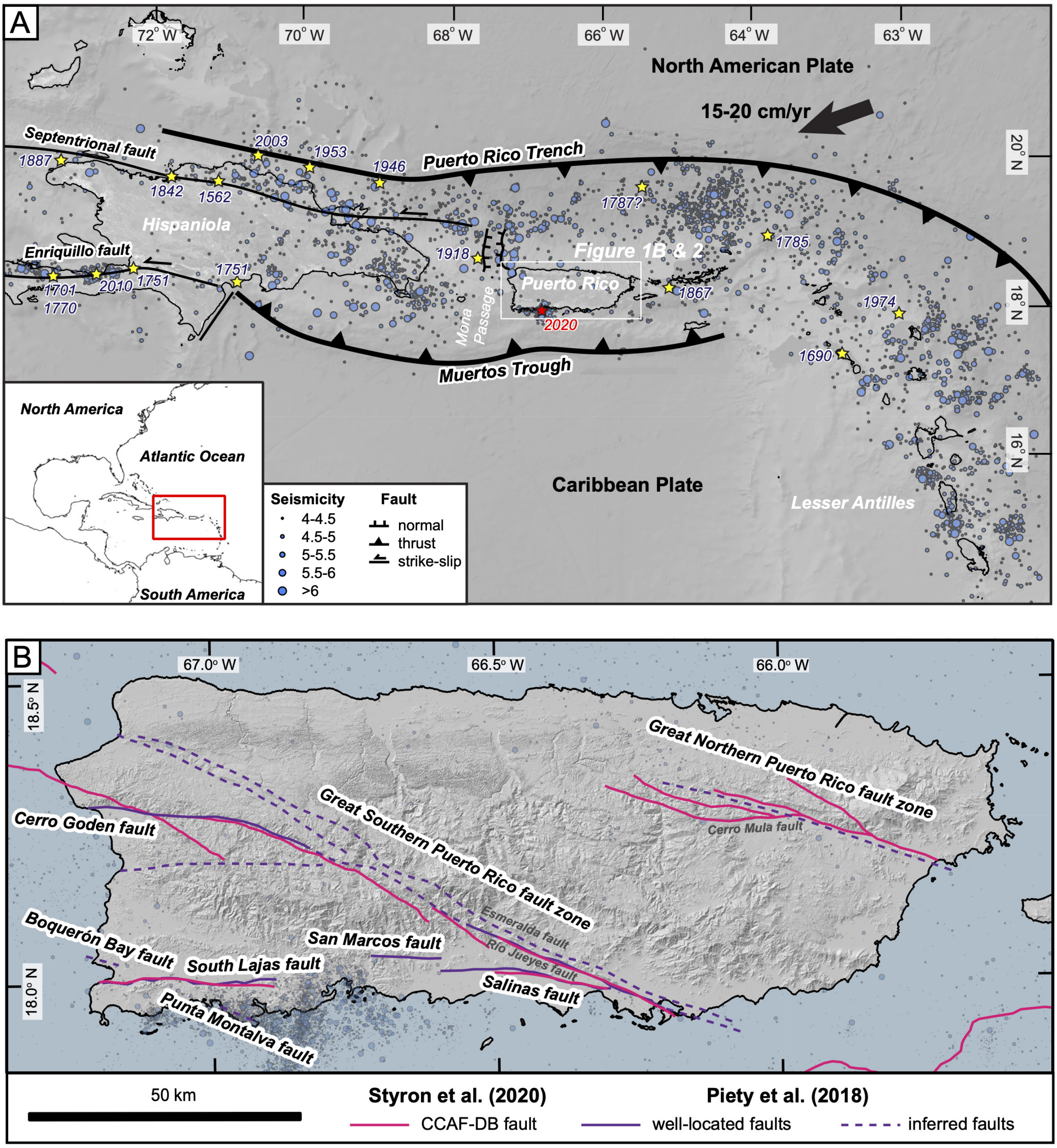

Figure 1 A) Tectonic setting of the northeast Caribbean. Global positioning system (GPS) arrows from Calais et al. (2016). The yellow stars mark the epicenters of magnitude $(M){>}7$ earthquakes in the historical and instrumental record, from ten Brink et al. (2011) and Calais et al. (2016). The red star marks the location of the moment magnitude $(\mathrm{M_w})$ 6.4 mainshock of the 2020 southwest Puerto Rico seismic sequence. Inset map shows the location of the Puerto Rico-U.S. Virgin Islands region in the northeast Caribbean. Background image is a GoogleEarth image converted to grayscale. (B) Past fault map compilations from Piety et al. (2018) and Styron et al. (2020) for Puerto Rico. Background image is a shaded relief map derived from the 10-m National Elevation Dataset digital elevation model (available at https://nationalmap.gov/). Seismicity shown in both panels is from the U.S. Geological Survey Advanced National Seismic System (ANSS) Comprehensive Catalog (U.S. Geological Survey, 2017). CCAF-DB—Caribbean and Central American Active Fault Database.

topographic data. Where possible, we extracted topographic profiles across the scarps and relied on existing limited age control to characterize fault activity within a categorical slip rate framework. In addition, we documented an exposure of the South Lajas fault and dated offset strata using optically stimulated luminescence (OSL) and radiocarbon dating. We present evidence for Quaternary fault activity on seven onshore faults, including the South Lajas, Salinas, Punta Montalva, Great Southern Puerto Rico, Cerro Goden, Parguera, and San Marcos faults. Our mapping forms the foundation for an updated Quaternary fault map of Puerto Rico.

2 Background

Puerto Rico sits along the 3200-km-long active North America-Caribbean plate boundary (Figure 1A), a dominantly left-lateral strike slip plate boundary (DeMets et al., 2000). Most of the plate boundary fault zone lies offshore and cannot be studied using traditional paleoseismic methods. Global positioning system (GPS) data within the stable, non-deforming Caribbean plate interior relative to North America shows that the Caribbean plate moves east-northeast (070°) at a rate of 18–20 ± 3 mm/yr (DeMets et al., 2000). Puerto Rico moves east-northeast at roughly the same rate as the larger Caribbean plate with differential motion between Puerto Rico and the island of Hispaniola accommodated by slow rifting in the Mona Passage (Jansma et al., 2000; Jansma and Mattioli, 2005). Oblique collision of the Bahama carbonate platform with Hispaniola has impeded eastward motion of Hispaniola relative to North America (Vogt et al., 1976; Mann et al., 1995; Dolan et al., 1998; Dolan and Wald, 1998) and produced a complex zone of rotational and extensional deformation in the Mona Passage.

Puerto Rico and the Virgin Islands move with the larger Caribbean plate, but internal deformation is locally observed (McCann and Pannington, 1990). Right-lateral motion on west-northwest-striking faults is predicted in Puerto Rico (Dolan et al., 1998; Dolan and Wald, 1998), and GPS data indicate that although little plate-boundary motion (<3 mm/yr) is accommodated within onshore Puerto Rico (Jansma et al., 2000), differential velocities between stations located on the southwest corner versus the central portion of the island show active deformation is focused along the southwestern corner of the island (Solares, 2019). Moreover, the 2019–ongoing southwest Puerto Rico seismic sequence supports this interpretation (e.g., Blasweiler et al., 2022; Yoon et al., 2023).

2.1 Recent Active Fault Maps

Several recent active fault compilations have summarized the existing literature on active and potentially active faults on the island, but none have included an island-wide reanalysis of the terrain using the newly acquired <1-m lidar data (U.S. Geological Survey, 2020). For example, Piety et al. (2018) mapped the south-central and southeastern portions of the island in detail using a DEM derived from lidar data, focusing on the Salinas and Great Southern Puerto Rico fault zones for a site-specific seismic hazard analysis. Piety et al. (2018) also evaluated the existing literature to create a preliminary map of active and potentially active faults across the island. The Caribbean and Central American Active Fault Database (CCAF-DB; Styron et al., 2020) also contains compiled faults for the island. The CCAF-DB focus was on Caribbean-wide seismic hazard, and for this purpose, faults were highly simplified. These previous active fault maps are broadly similar (Figure 1B).

3 Methods

To identify and assess possible tectonic deformation in Puerto Rico, we mapped lineaments and fault-related features on a publicly available <1-m bare-earth lidar DEM and derivative visualizations, collected post-Hurricane Maria in 2018 and published through the USGS 3D Elevation Program in 2020 (U.S. Geological Survey, 2020, https://apps.nationalmap.gov/downloader/). Derivative visualizations of the landscape, such as slope and shaded relief models at different illumination and azimuth angles (Table S1), were analyzed, as some subtle features were more visible on different renderings. To complement the lidar mapping, we mapped fault-related features on historical aerial photos as well. The aerial images primarily covered the Cerro Goden, San Marcos, Salinas, and Parguera faults, where extensive recent anthropogenic development obscured the original topography in the lidar data. Aerial photos from the 1950s and 1960s are publicly available on EarthExplorer (https://earthexplorer.usgs.gov/), and those from the 1930s are available at https://prgeoref.weebly.com/1930-y-1936.html (López Marrero et al., 2017). We manually georeferenced the aerial photos from the 1950s and 1960s using common tie points between historical and present-day imagery and the lidar. We mapped fault-related features from the aerial imagery because of the excellent visual coregistration with the lidar (typically less than 10 m, but up to 50 m for registration errors). Aerial photos from the 1930s were already georeferenced and coregistration with the lidar was highly variable with coregistration errors between 10 and 30 m; thus, we mapped fault-related features when we were confident the lidar and aerial images were closely coregistered.

Mapped fault-related features include scarps, vegetation and tonal contrasts and lineaments, channel deflections, linear drainages, planform changes, and topographic lineaments. Mapped scarps are assumed to have formed by fault displacement. We defined correlative surfaces by similar surficial slopes on the upthrown and downthrown sides and similar surficial characteristics observed during fieldwork. We visually fit lines through the upthrown and downthrown surfaces and measure scarp vertical separation at the midpoint of each scarp. For each fault, we estimate vertical and lateral kinematics based on field observations and remote mapping. However, we caution that exact fault kinematics remain unknown for most faults, and even small changes in the orientation of faults may result in apparently large vertical displacements even if the

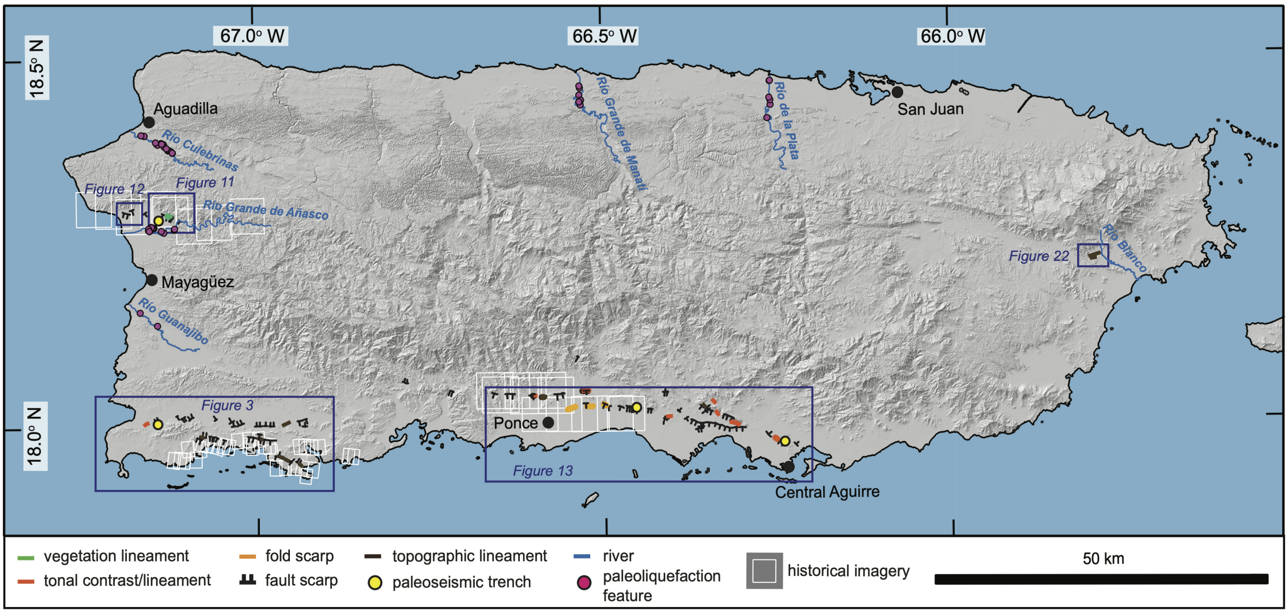

Figure 2 Fault-related features in Puerto Rico, newly mapped in this study and compiled from previous literature (Geomatrix Consultants, 1988; Mann et al., 2005; Prentice and Mann, 2005; Roig-Silva, 2010; Roig-Silva et al., 2013; Piety et al., 2018). Paleoliquefaction features are from Tuttle (2006). Background image is a shaded relief map derived from the 10-m National Elevation Dataset digital elevation model (available at https://nationalmap.gov/)

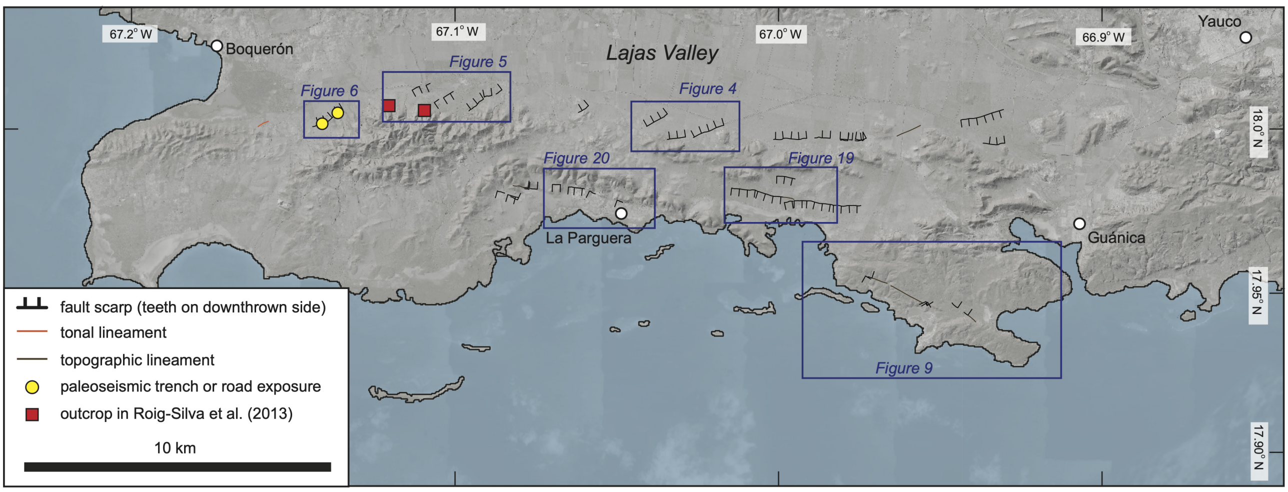

Figure 3 Overview of fault-related features mapped in southwestern Puerto Rico. Location shown on Figure 2. Background image is a blend of GoogleEarth imagery converted to grayscale overlain on a shaded relief map derived from the <1-m lidar elevation data.

fault is dominantly strike-slip (e.g., Ridgecrest, California, surface ruptures, DuRoss et al., 2020). These fault-related features were then classified into pre- Quaternary bedrock faults if we did not observe offset Quaternary deposits, and Quaternary-active faults if the fault displaces Quaternary deposits visible in the lidar-derived topography and/or Quaternary deposits shown on existing geologic and geomorphic maps. We field-verified the mapping of neotectonic features along all faults, including making observations of fault scarp vertical separation, scarp aspect, ages of deposits, and general landscape characteristics.

We also logged and interpreted an outcrop exposure of the South Lajas fault. We used standard structure-from-motion techniques to create a three-dimensional (3D) model of the exposure wall, following the workflow described in Reitman et al. (2015) and Delano et al. (2021). We described units following Schoeneberger et al. (2012) (Table S2) and collected four optically stimulated luminescence (OSL) and six radiocarbon (^{14}C) samples to constrain the ages of the units. OSL dating was performed on quartz sand (90–250 µm), and reported ages follow the Central Age Model (Galbraith et al., 1999) reported to 2σ. Additional details for the ^{14}C dating can be found in Tables S3 and S4. Additional details for the OSL sampling and dating can be found in Table S5 and Mahan et al. (2024).

4 Results

We mapped more than 134 fault-related features, which we associate with active faults or zones of active deformation that clearly offset or deform Quaternary deposits (Figure 2). Scarps and neotectonic features are concentrated near coastlines and in river valleys where Quaternary deposits are preserved (Figure 2). Most scarps are <1 km in length and sinuous. Topographic lineaments observed in steeper topography, with a likely bedrock control, are up to several kilometers long. Our mapping defined seven onshore faults that agree broadly with prior fault compilations (e.g., Piety et al., 2018; Styron et al., 2020). However, new mapping provides higher resolution fault location and geometry. Below, we briefly describe the remote mapping observations from lidar-derived topography and historical aerial photos, with supporting field measurements where we were able to access and document the fault-related features.

4.1 South Lajas fault

The South Lajas fault (Prentice and Mann, 2005) is an east–west-trending fault located in southwestern Puerto Rico, along the southern edge of the Lajas Valley (Figure 1B). Mapping from <1-m lidar-derived topography has shown that the South Lajas fault can be traced at the surface for nearly 24 km along the southern Lajas Valley (Figure 3). A series of en echelon east-to northeast-trending fault scarps with primarily down-to-the-north/northwest but also down-to-the-southeast senses of motion mark the surface expression of the fault. Scarps are 1- to 3-m tall with lengths from 200 m to 1 km.

Where observed in the field, the scarps vertically offset young alluvial surfaces by <3 m. At the eastern end of our mapping in the Lajas Valley, the scarp is <2-m tall and faces north to northwest (Figure 4). To the east beyond these clear scarps, several subtle breaks in slope and <20-cm-tall southwest-facing and northeast-facing scarps with a similar orientation (east– northeast- to east-trending) are visible in the lidar-derived shaded relief and slope maps crossing several fields. We base our interpretation of the eastern limit of the South Lajas fault on these small scarps.

Offset alluvial deposits have been documented at several locations along the South Lajas fault. A documented gully exposure displays vertically aligned pebble to cobble-sized clasts (Figure 5; Roig-Silva, 2010). Another vertical exposure of northeast-trending normal faults is ~1.5 km to the west in the Laguna Cartagena National Wildlife Reserve and shows alluvial sediments displaced by up to 33 cm (Figure 5; Figure 6 in Roig-Silva et al., 2013). A ground penetrating radar (GPR) profile near this exposure documents subsurface offset of reflectors, interpreted to be faults, but the faults do not appear to displace the surface sediments in the stream (Roig-Silva et al., 2013). These observations of northeast-trending normal faults, vertically aligned clasts within gullies, and offset subsurface reflectors on GPR profiles correlate with mapped scarps on the lidar-derived topography, although the faults generally have a down-to-the-north sense of motion in GPR profiles whereas the scarps mapped from lidar have a down-to-the-south sense of motion. This difference in apparent displacement may result from a lateral component of slip during recent surface-faulting events that would juxtapose units of different thicknesses or facies against each other.

Parts of the Lajas Valley have closed depressions, shallow lagoons, and wetlands, all of which may have held shallow ephemeral lakes in the past (i.e., Figure 5; Laguna Cartagena, Guánica Lagoon, Ríos et al., 2012). However, we do not interpret observed scarps here to be lacustrine-related because of their variable elevation and the fact that they are unique to the southern side of the Lajas Valley. Lacustrine-related features would maintain consistent elevations and would likely be present throughout the entire valley. Moreover, the scarps have an en echelon pattern, unlike typical shorelines in valleys.

Based on this evidence, we interpret that the South Lajas fault is characterized by en echelon scarps that extend for ~24 km along the southern side of the Lajas Valley. Shallow subsurface evidence of the fault has been documented in at least four locations along strike (Prentice and Mann, 2005; Roig-Silva, 2010; Roig-Silva et al., 2013, this study).

4.1.1 South Lajas Fault - Guanabanas Road Exposure

The South Lajas fault is visible in outcrop where one of the scarps associated with the fault intersects a road (Figure 6). We documented this outcrop to corrobo-

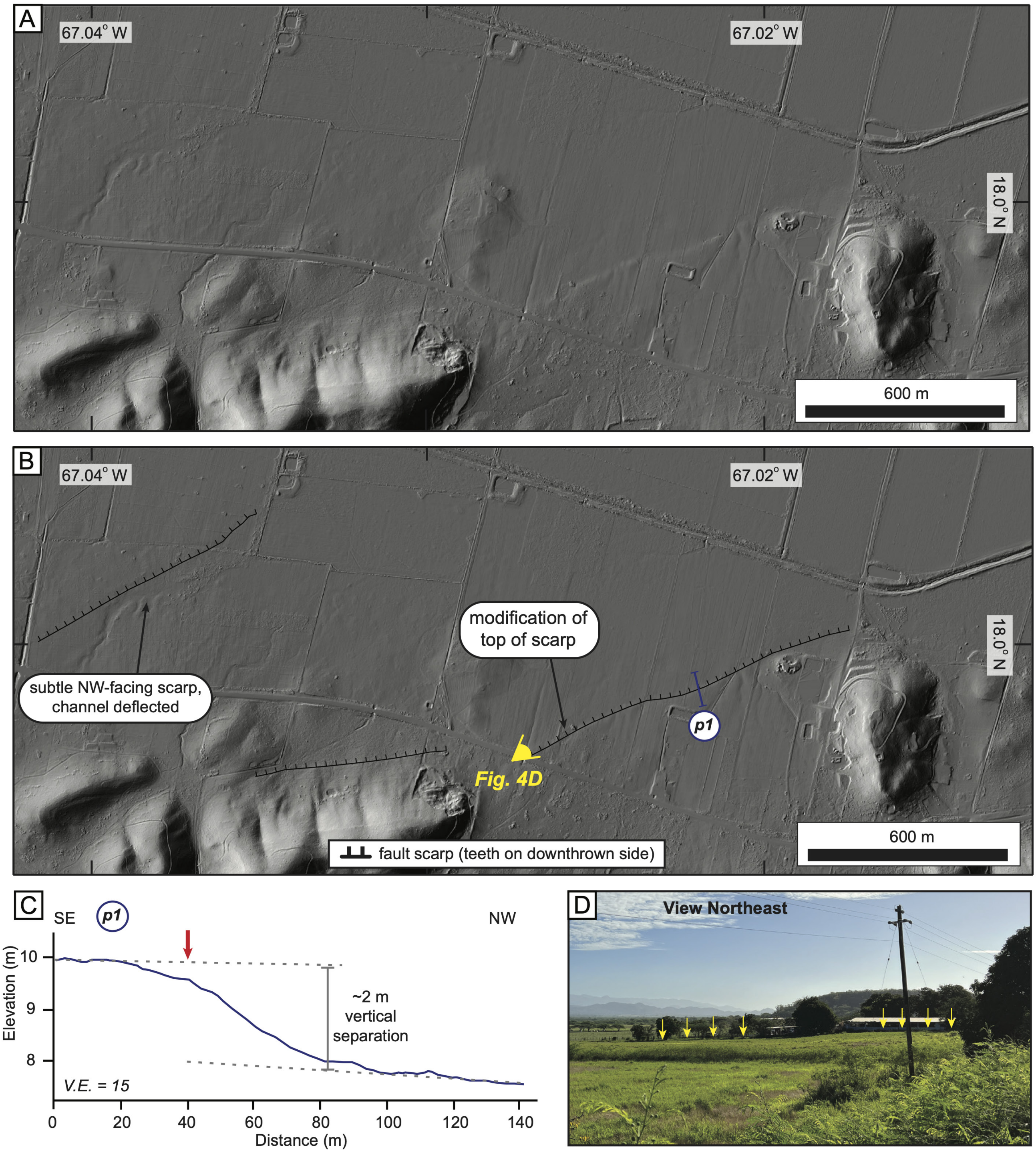

Figure 4 (A) Uninterpreted and (B) interpreted shaded relief map of the eastern extent of the South Lajas fault derived from the 1-m lidar data. Location in Figure 3. (C) Topographic profile of a scarp from southeast (SE) to northwest (NW), indicating ~2 m of vertical separation. Red arrow marks the top of the scarp mapped in the lidar-derived topography. V.E.—vertical exaggeration. (D) Field photograph, looking northeast along the scarp. Yellow arrows mark the top of the surface.

rate the paleoseismic trench observations from Prentice and Mann (2005), who trenched the same scarp ~500 m along strike to the southwest. At the road outcrop, the fault scarp is 1.5-m tall, and intersects the road at a high angle. The exposure is 25.3-m long and 5.1-m tall. The road is set into the surface, so the height of the exposure appears taller than the scarp visible on the surface.

We described and interpreted four sedimentary units in the exposure (Table 1, Figure 7, and Table S2). Unit 1 is located at the eastern end of the exposure. It is a brown, angular to subangular pebble-cobble clast-supported unit, with weak bedding. The lowermost part is more clast-supported and was partially obscured by slope colluvium at the time of our visit. Unit 2 and Unit 1 are separated by a smooth, continuous contact. Unit 2 generally has smaller angular clasts (pebble-sized) and is more matrix-supported. The modern soil is developed atop Unit 2 and has a wavy lower boundary with the parent material. This soil is fine-grained and contains abundant clays and carbonate horizons. Although the O and A soil horizons were obscured by the exposure height and cover on the eastern side of the exposure, a coarse blocky B/Bk horizon with stage I carbonate (Gile et al., 1966) extended through most of the section. Unit 3 is located at the western end of the exposure. It is a brown subrounded to subangular pebble matrix-supported unit, with weak bedding, and the lowermost part of the unit is covered by colluvium. The upper part of Unit 3 is well indurated, fine-grained, and contains clays and carbonate horizons. The top of Unit 3 is a reddish-tan soil, with a wavy lower contact. Unit 4 is located at the top of the exposure. It is dark brown, moderately indurated, and has more silt with uncommon pebbles. Within Unit 4, we observed extensive bioturbation and two pieces of ceramic material. We interpret that Units 1–3 were deposited in an alluvial fan environment, with the upper part of Unit 1 and Unit 2 broadly correlating with Unit 3, although no marker beds or distinct features could be correlated across the outcrop. Unit 4 is a colluvial package that was deposited at the base of the scarp.

Because of the highly oblique angle between the fault and the roadcut, we observe the fault plane itself in the exposure, and the apparent geometry of the fault at this angle is anastomosing and sub-vertical. The subvertical fault trace and facies mismatch between fan units indicate a substantial component of oblique slip on the fault. We also interpret additional fissures ~2 m east of the primary fault (Figure 7), but it is unclear if these formed during the same or a different paleoearthquake.

All six radiocarbon samples yielded modern ages (Table 2). This result is unexpected, given the in situ nature of the samples collected. We suspect the charcoal samples may be modern material that moved into the profile through fissures and bioturbation. Although we were careful to sample in areas apparently free from bioturbation, there is evidence for bioturbation deep in the section, and ground fissures and cracking between peds in the soil profile may have led to deep infiltration of younger material. The modern ages in the uppermost units (sample RC-6; Unit 4 colluvial wedge) agree with observations of extensive bioturbation and ceramic material.

OSL ages date the deposition of the alluvial fan units (Units 1-3) to late Pleistocene (33-15 ka; Table 3; refer to Supplementary Material Table S5 and Mahan et al., 2024). The overlying colluvial deposit is dated to 3.9 ka. Quartz was not abundant in the samples, and some of the samples only yielded enough material for three aliquots, leading to large uncertainties in the equivalent dose and resulting sample age.

4.1.2 South Lajas fault history

We interpret a single paleoearthquake from the exposure, similar to what was observed in the paleoseismic trench (Boquerón) by Prentice and Mann (2005), who interpreted one Holocene earthquake approximately 5,000 years ago based on limited radiocarbon ages of the youngest faulted deposits.

Constraining the age of the most recent event remains challenging. Using the four OSL ages from the Guanabanas road exposure, the most recent earthquake likely occurred between 4 and 15 ka. However, the paleoseismic trench described in Prentice and Mann (2005) is only 500 m to the southwest. If we assume that the units are broadly correlative and the same earthquake ruptured to the surface at each trench, then the paleoearthquake timing can be more tightly constrained to <~5 ka (youngest faulted deposits at Boquerón trench; Prentice and Mann, 2005) and >4 ka (age of colluvium overlying fault scarp at Guanabanas exposure) (Figure 8).

The simplest interpretation of the Guanabanas road exposure is that it records a single event; a recurrence interval cannot be determined but is likely >20 kyr if the OSL ages of the fan deposits are 33 ka. Given the relative lack of dated faulted and unfaulted deposits in the Guanabanas road exposure and the Boquerón trench of Prentice and Mann (2005), the recurrence interval of surface rupturing earthquakes on the South Lajas fault remains an open question. Using an estimated age of the surface of ~10 ka (radiocarbon ages of 5-7.5 ka, Prentice and Mann (2005); OSL ages of ~15 ka, this study) and a maximum vertical separation of ~3 m, the South Lajas fault has a vertical slip rate of ~0.3 mm/yr. Using the maximum and minimum possible ages yields a range of vertical slip rates between 0.2 and 0.6 mm/yr. However, given the evidence for an unknown lateral component as observed by the mismatch of alluvial fan units across the fault at both the Guanabanas road exposure and in the Boquerón trench and the en echelon stepping pattern of the scarps, the rate of ~0.3 mm/yr is likely a minimum slip rate.

4.2 Punta Montalva fault

The Punta Montalva fault is a northwest–southeast-trending fault in southwestern Puerto Rico (Figure 1B and Figure 9). The fault clearly offsets Oligocene and Miocene units, including the late Tertiary (~15 Ma) Ponce Limestone (Roig-Silva et al., 2013). Shallow geophysical data document a fault in the subsurface (Adames-Corraliza, 2017). Using GPR and boreholes, Adames-Corraliza (2017) interpret that the base of the

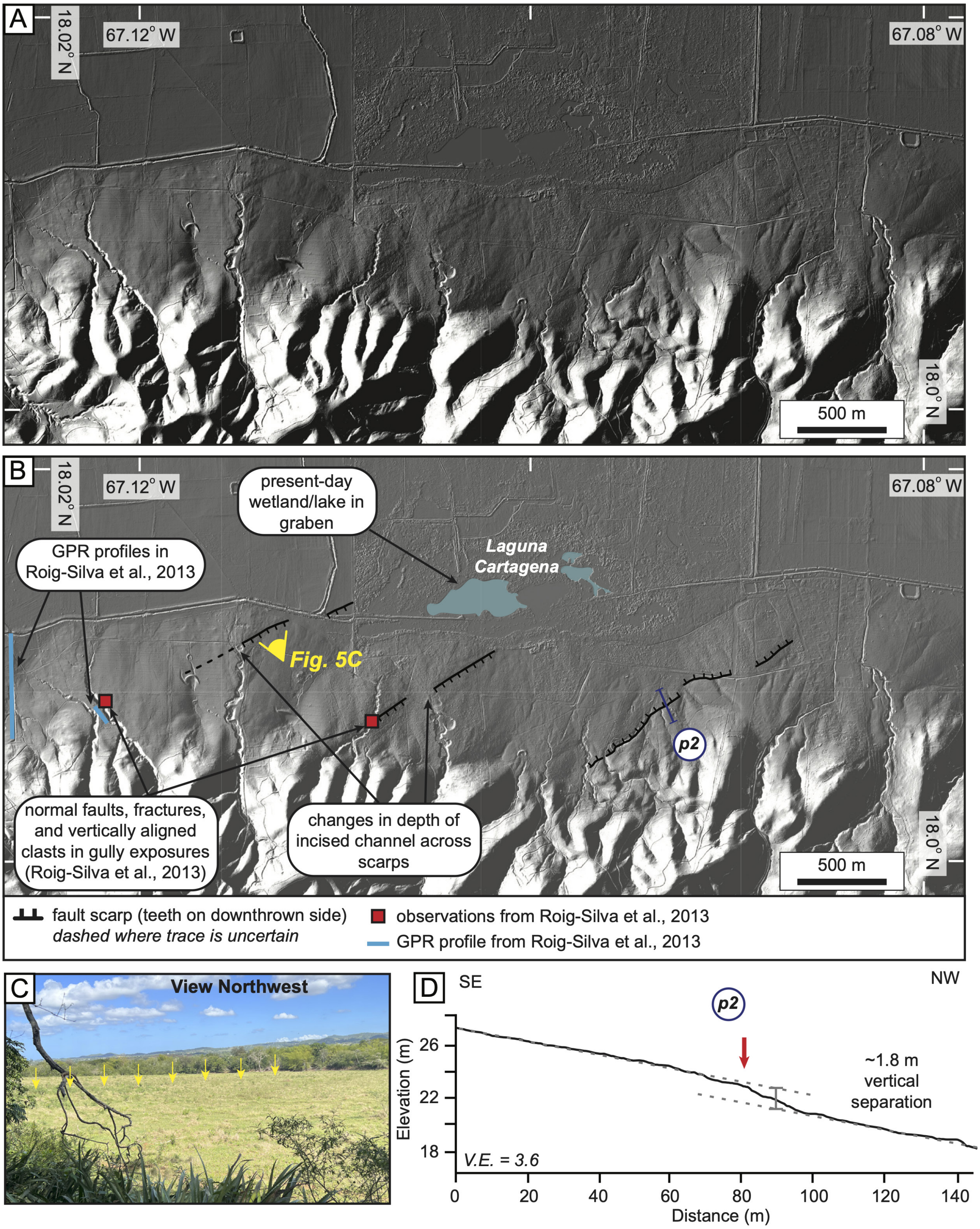

Figure 5 (A) Uninterpreted and (B) interpreted low-angle shaded relief map of the central South Lajas fault derived from 1-m lidar data. Location in Figure 3. (C) Field photograph, looking northwest (NW) along the scarp. Yellow arrows mark the top of the surface. (D) Topographic profile of a scarp from southeast (SE) to NW, indicating ~1.8 m of vertical separation. Red arrow marks top of scarp mapped in the lidar-derived topography. GPR—ground penetrating radar; V.E.—vertical exaggeration.

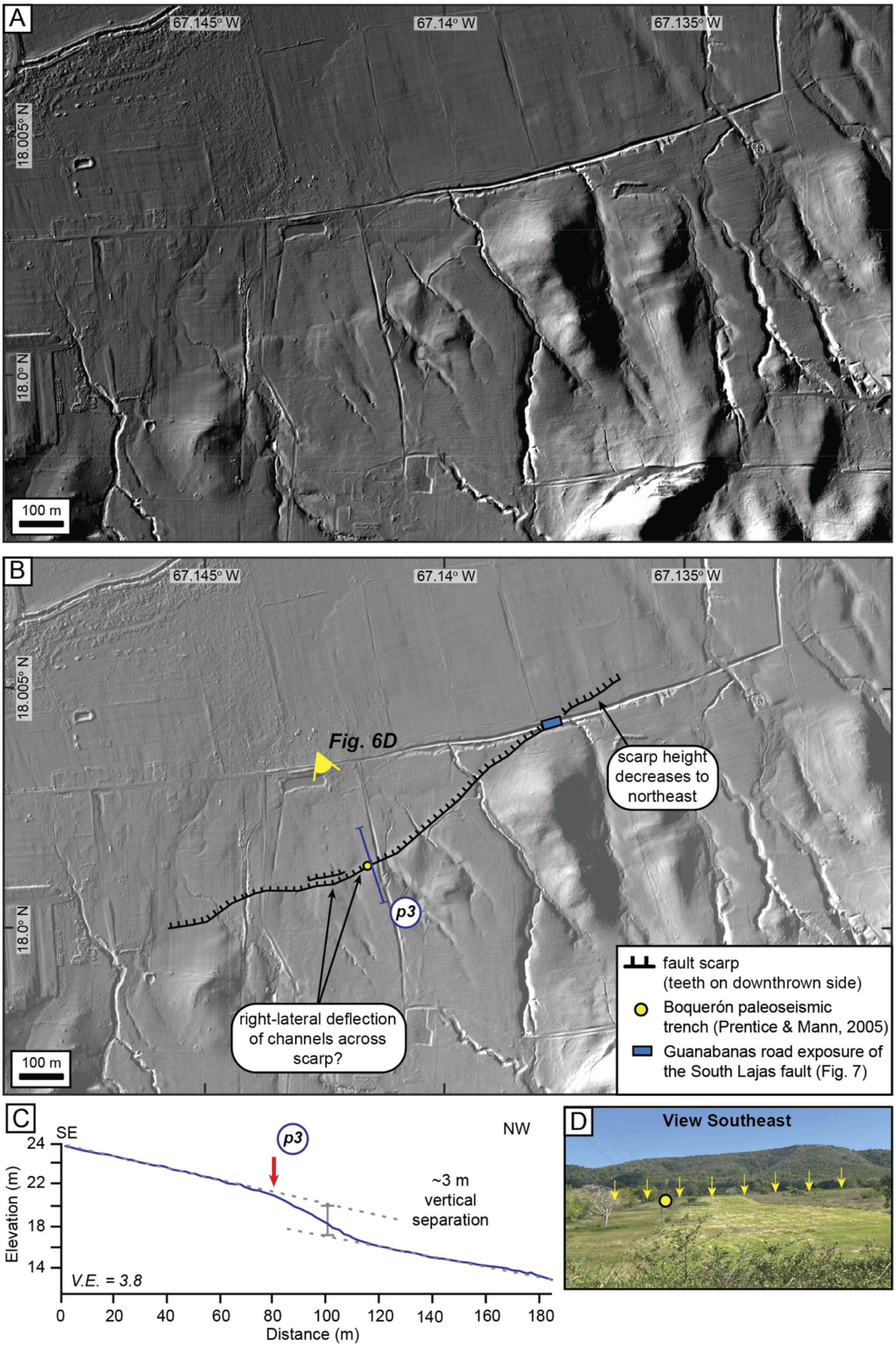

Figure 6 (A) Uninterpreted and (B) interpreted low-angle shaded relief map of the central South Lajas fault derived from 1-m lidar data. Location in Figure 3. (C) Topographic profile of a scarp from southeast (SE) to northwest (NW), recording ~3 m of vertical separation. Red arrow marks top of scarp mapped in the lidar-derived topography. V.E.—vertical exaggeration.(D) Field photograph, looking southeast toward the scarp. Yellow arrows mark the top of the surface. Yellow circle marks the location of the paleoseismic trench from Prentice and Mann (2005).

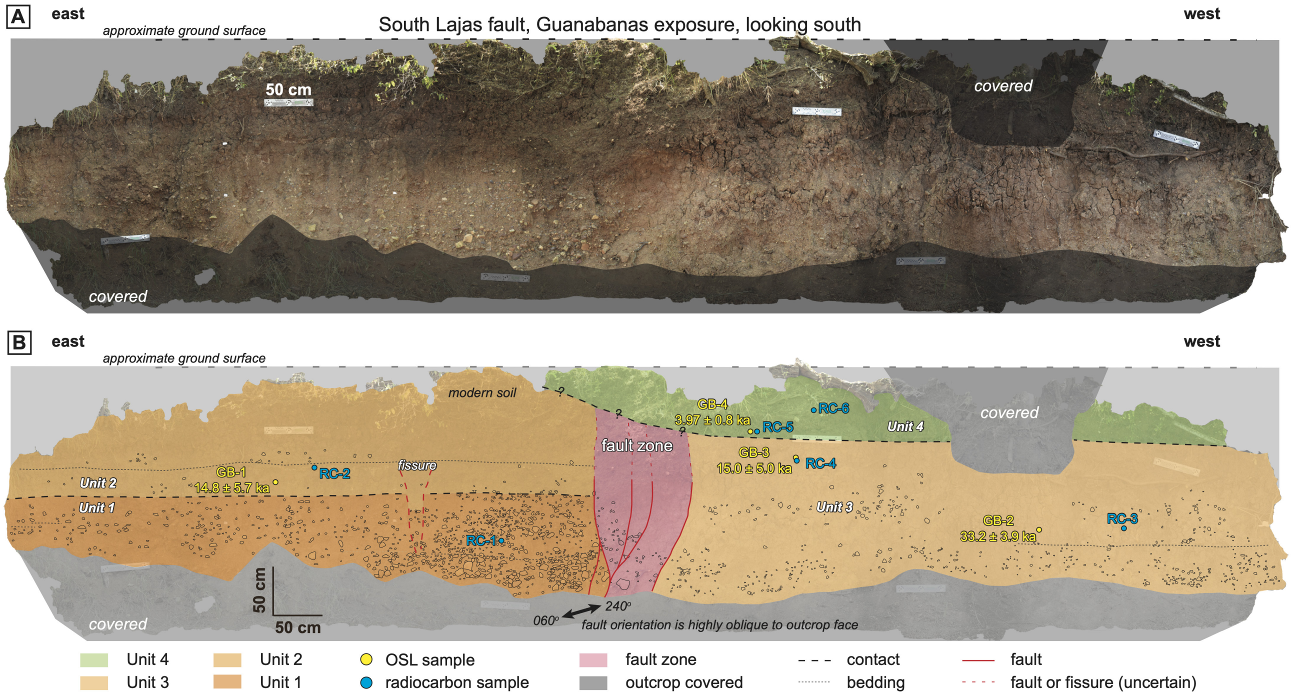

Figure 7 Guanabanas road exposure of the South Lajas fault orthomosiac photo derived from structure-from- motion and interpretation. Location in Figure 6. Unit descriptions are in Table 1 and Table S2, and optically stimulated luminescence (OSL) ages are in Table 3. Radiocarbon ages are not shown on the figure because all radiocarbon samples returned modern ages (refer to Table 2, Tables S3 and S4).

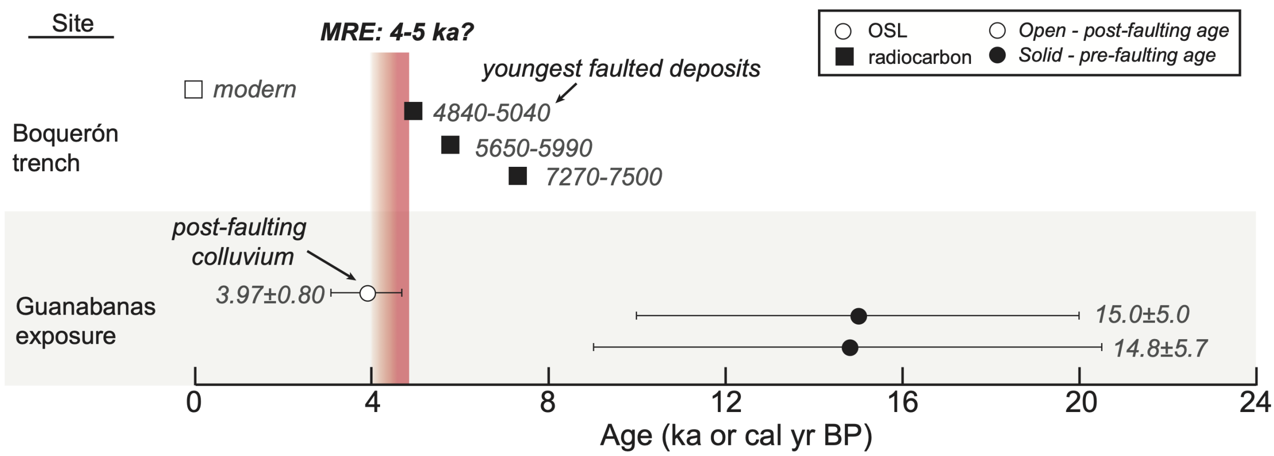

Figure 8 South Lajas faulting history, integrating ages and observations from this study (Guanabanas road exposure) and Prentice and Mann (2005) (Boquerón trench). If units are broadly correlative, the most recent event (MRE) is likely between 4 and 5 ka. cal yr BP—calibrated years before present; ka—thousand years ago; MRE—most recent earthquake.

Unit Number	General Description	Interpretation
1	Angular to subangular clast-supported pebble-cobble conglomerate, weakly bedded, brown	Alluvial fan
2	Angular matrix-supported gravelly coarse sand, very weakly bedded, uppermost part is fine-grained with clays and discontinuous carbonate horizons, brown. Modern soil developed at top of unit	Alluvial fan
3	Angular matrix-supported gravelly coarse sand, weakly bedded, brown. Top of unit is well-indurated, fine-grained, matrix-supported with uncommon pebble clasts, discontinuous carbonate horizons	Alluvial fan
4	Dark brown silty sand, uncommon angular clasts, massive bedding	Colluvial (wedge)

Table 1 Generalized unit descriptions for the Guanabanas road exposure on the South Lajas fault. Refer to Supplementary Material for more detailed unit descriptions in Table S2.

14C sample number	Depth (m)	Organic identification and notes	Age (yrs)
GB-RC-1	1.8	1 wood fragment	>Modern
GB-RC-2	1.5	4 wood fragments	>Modern
GB-RC-3	1.6	6 wood fragments	>Modern
GB-RC-4A	0.9	1 charcoal fragment	195 $\pm$15
GB-RC-4B	0.9	1 woody fragment (rootlet?)	>Modern
GB-RC-5	0.6	45 charcoal fragments, found pottery shard within sample	195 $\pm$15
GB-RC-6	0.4	5 charcoal fragments	205 $\pm$15

Table 2 Radiocarbon (^{14}C) sample data for the Guanabanas road exposure on the South Lajas fault. Refer to Supplementary Material for more details on plant and wood identification and analytical measurements in Tables S3 and S4.

soil is deformed across a mapped Quaternary deposit near the center of the fault with an apparent 0.9-m-deep graben. Three ruptures are interpreted from the formation of the graben and deformation of the base of soil, with a recurrence interval of 3300 years, assuming a Holocene (~10 ka) age for the alluvial deposits based on fossil identification within a surface soil sample (Adames-Corraliza, 2017). Recent mapping on lidar-derived topography has constrained left-lateral offset of an undated, intermittent channel to ~133 m (Weilert and Laó-Dávila, 2023). It is not clear how much of the ~133 m apparent offset of the prominent channel is possible deflection versus tectonic offset. Offshore to the southeast, mapping on high-resolution bathymetry indicates ~4.8 m of down-to-the-north vertical separation and up to 98 m of left-lateral offset of a reef (Weilert and Laó-Dávila, 2023) that may be Holocene in age based on correlation of other reefs on the Parguera insular shelf (Morelock et al., 1994; Hubbard et al., 1997).

In the lidar-derived topography, the Punta Montalva fault is expressed as a sharp topographic lineament that trends ~285°. Limestone bedrock crops out along most of the Punta Montalva fault and is responsible for the strong topographic expression of the fault. Along the southern section, the fault is expressed as a prominent bedrock scarp that is 1.5- to 2-m tall, with flat-lying limestone units present in the hanging wall. Several small, ponded basins are present along the length of the fault (Figure 9).

There are few young, potentially Holocene, alluvial surfaces that preserve recent faulting. From the lidar-derived topography, we mapped and field-checked several locations where the fault may offset younger alluvial surfaces. At the southeastern end of the fault, several alluvial surfaces preserve scarps that are ~20 cm to 1.5 m tall. At site A (Figure 9 and 10), en echelon scarps that are slightly oblique to the main trace of the fault trend 310–330°, are 20–40 cm tall and face both northwest and southeast. However, the origin of these scarps remains unclear, and they may be fluvial features or mantled bedrock features that are in the shallow subsurface.

These scarps are within the same ponded basin studied by Adames-Corraliza (2017), who concluded that the base of the soil is deformed across these faults. Approximately 500 m to the east, in an alluvial deposit that has been heavily modified from agricultural activity (site B), a small 25-cm-tall northeast-facing scarp is observed in the lidar-derived topography across two fields and the road (Figure 10); field observations corroborate a small northeast drop in the road, but because of thick vegetation in the fields and substantial anthropogenic modification of the surface, we were unable to confirm the presence of the scarp beyond the road. Near the northwestern end of the fault (site C on Figure 9), there is a small broad uphill-facing scarp across ponded alluvium.

The presence of scarps with opposite facing directions and en echelon patterns, coupled with the apparently left-laterally offset channel and linear geomorphic expression, support the interpretation that the fault is likely primarily strike-slip with a down-to-the-northeast vertical component. Although the alluvial surfaces are undated, the expression of small (<0.5 m) scarps in these young surfaces supports the designation of a late Pleistocene or Holocene fault activity.

Moreover, the fault location and left-lateral kinematics observed in the landscape agree with seismicity (epi-

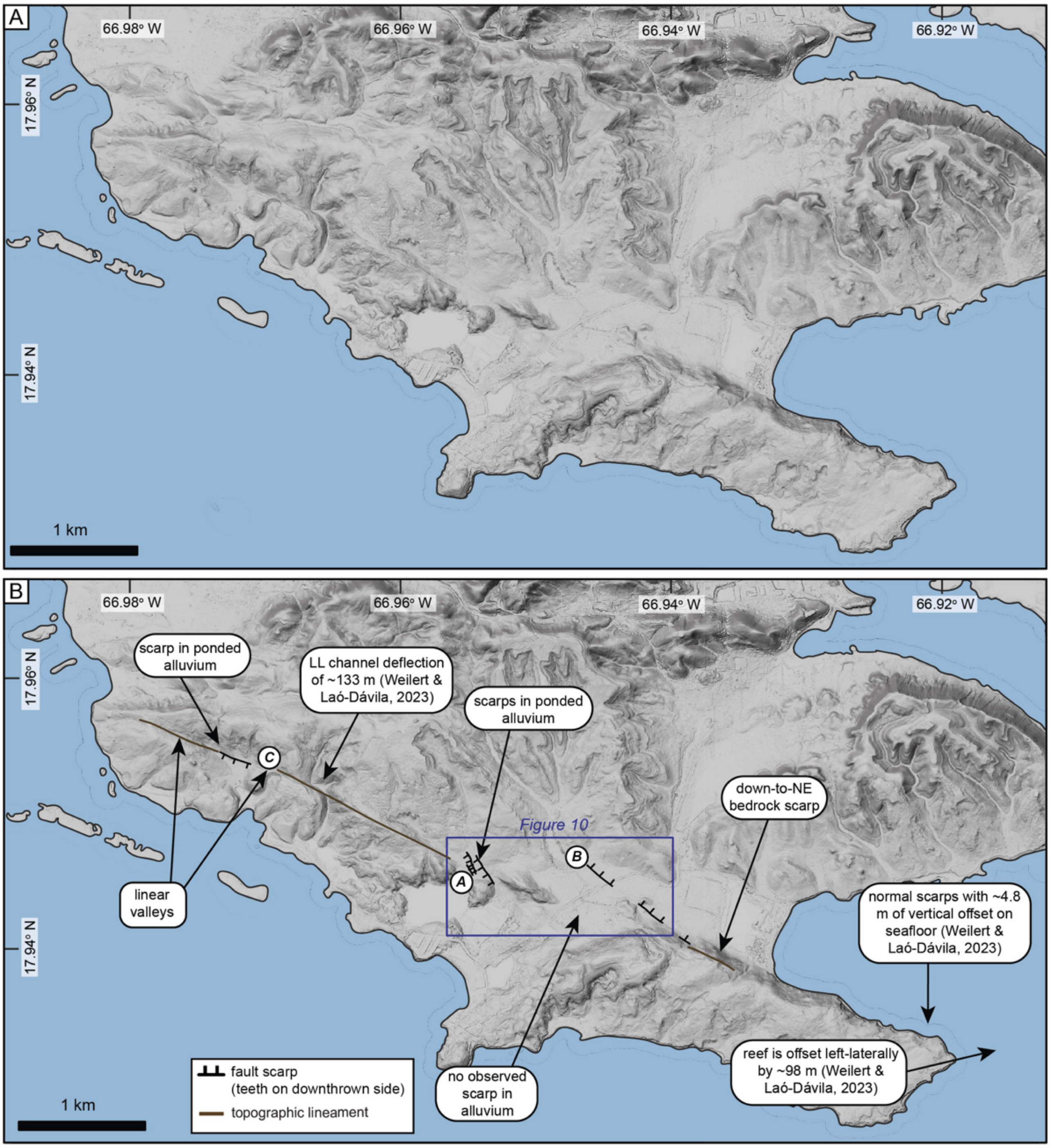

Figure 9 (A) Uninterpreted and (B) interpreted slope map of the Punta Montalva fault derived from 1-m lidar data. Location in Figure 3. LL—left lateral; NE—northeast. Circled letters are sites described in text.

OSL sample number	Depth (m)	Water Content[a] (%)	K[b] (%)	U[b] (ppm)	Th[b] (ppm)	Dose Rate[c] (Gray/Ka)	n[d]	over dispersion	CAM D_e[e] (Gray)	CAM Age (ka)
GB-1	1.1	6	0.87 ± 0.017	0.48 ± 0.014	1.56 ± 0.08	1.02 ± 0.03	3(3)	0 %	15.0 ± 5.8	14.8 ± 5.7
GB-2	1.6	10	0.74 ± 0.015	0.59 ± 0.018	1.77 ± 0.09	0.89 ± 0.03	15(37)	42 %	29.4 ± 3.4	33.2 ± 3.9
GB-3	0.9	10	0.67 ± 0.013	0.65 ± 0.02	2.42 ± 0.12	0.88 ± 0.02	6 (15)	79%	13.3 ± 4.4	15.0 ± 5.0
GB-4	0.6	10	0.77 ± 0.015	0.60 ± 0.018	2.28 ± 0.11	0.96 ± 0.03	11(35)	64%	3.81 ± 0.76	3.97 ± 0.80

Table 3 Optically stimulated luminescence (OSL) sample data for the Guanabanas road exposure on the South Lajas fault. [a] Refer to Mahan et al. (2024) for additional notes on Water Content Calculations. [b] K, U, and Th determined by high-resolution Ge gamma spectroscopy or inductively coupled plasma mass spectrometry (ICP-MS). [c] Environmental Dose Rate, calculated using the Dose Rate Age Calculator (Durcan et al., 2015). [d] Number of aliquots meeting acceptance criteria, total number of aliquots measured in parentheses. [e] CAM – Central Age Model calculated following. Galbraith et al. (1999); Refer to Mahan et al. (2024) for additional details.

center locations and focal mechanisms) observed during the 2019-ongoing seismic sequence (e.g., Blasweiler et al., 2022; Yoon et al., 2023).

4.3 Cerro Goden fault zone

The Cerro Goden fault zone is located in western Puerto Rico and generally strikes east and dips south (Figure 1B). It is associated with a topographic lineament along the base of Cerros de San Francisco mountains and in Añasco Valley (McIntyre, 1971). Offshore, the fault is mapped based on offset seafloor sediments estimated to be late Quaternary age (Grindlay et al., 2005). The fault has previously been proposed to be Quaternary active, but definitive evidence of Quaternary activity remains elusive. Using aerial photos, Mann et al. (2005) identified aligned and deflected drainages, offset terrace risers, and uphill facing scarps. Six paleoseismic trenches revealed limited evidence of surface rupture, although a mountain-facing paleoscarp is visible in the subsurface with unfaulted Holocene fluvial sediments against the paleoscarp (Zachariasen and von Hillebrandt-Andrade, 2005). At one trench (ES1), the overlying unfaulted alluvium had conventional radiocarbon ages of 3890±40 yr BP and 2330±40 yr BP (calibrated age ranges of 2470–2200 B.C. and 420–370 B.C., respectively; Zachariasen and von Hillebrandt-Andrade (2005). Trench ES2 revealed subtle evidence of Holocene faulting, including vertically rotated pebbles, truncation of beds, and progressive deformation of Holocene units with proximity to the interpreted fault and uphill facing scarp. However, Zachariasen and von Hillebrandt-Andrade (2005) presented an alternative interpretation of the apparent uphill facing scarp as a buttress unconformity based on clays that were not offset at the base of the trench. Another trench revealed unfaulted sediment <1000 years old, although these paleoseismic trenches do not coincide with any obvious scarps in the lidar data. Paleoliquefaction features from the Río Grande de Añasco and Río Culebrinas (Figure 2) date to 1300–1508 A.D. and >1670 A.D. and are interpreted as the result of a M>6.5 earthquake on the Cerro Goden or other unknown or offshore fault (Tuttle et al., 2005).

From the lidar-derived topography, we mapped scarps and topographic lineaments that generally trend east–west with a down-to-the-south sense of displacement (Figure 11, Figure 12). Many of these scarps have been modified by development over the last several decades and are now preserved as prominent steps of up to 5 m between rows of houses (Figure 11C). Farther east, along the Río Grande de Añasco, a terrace displays potential backtilted geometry along the trace of the fault (Figure 11D). To the west, smaller sinuous, discontinuous scarps (<1.5-m tall) face south and are modified by human development. At least one of these scarps coincides with a prominent vegetation lineament in the historical imagery (Figure 11B). Field-verification of the scarps was challenging due to landscape modification and thick vegetation, but prominent topographic steps in heavily developed areas coincide with the mapped scarps on the lidar data.

Clear evidence of late Pleistocene or Holocene activity of the Cerro Goden fault remains equivocal, in part because of the extensive landscape modification along the most prominent topographic scarps and the lack of dated faulted surfaces. However, the presence of topographic scarps across alluvial fans and terraces (this study), changes in channel planforms, concentrations of paleoliquefaction features (Tuttle et al., 2005), and changes in landscape metrics (e.g., normalized channel steepness, chi, and asymmetry factor) (Galíndez, 2018) indicate some Holocene activity on the fault. Offshore to the west, the Cerro Goden fault is interpreted to be Holocene-active based on displaced reefs in Bahía de Mayagüez (Grindlay et al., 2005).

Using a scarp vertical separation of ~1.4 m (the maximum scarp height observed that is not extensively modified; Figure 12D) and assuming a maximum 10 ka age for the alluvial plain deposits, we calculate a vertical separation rate of 0.14 mm/yr. The Cerro Goden has been proposed to have a right-lateral component (Mann et al., 2005; Grindlay et al., 2005), but without clearly offset geomorphic markers, we cannot determine the lateral slip rate; thus, this rate is likely a minimum fault

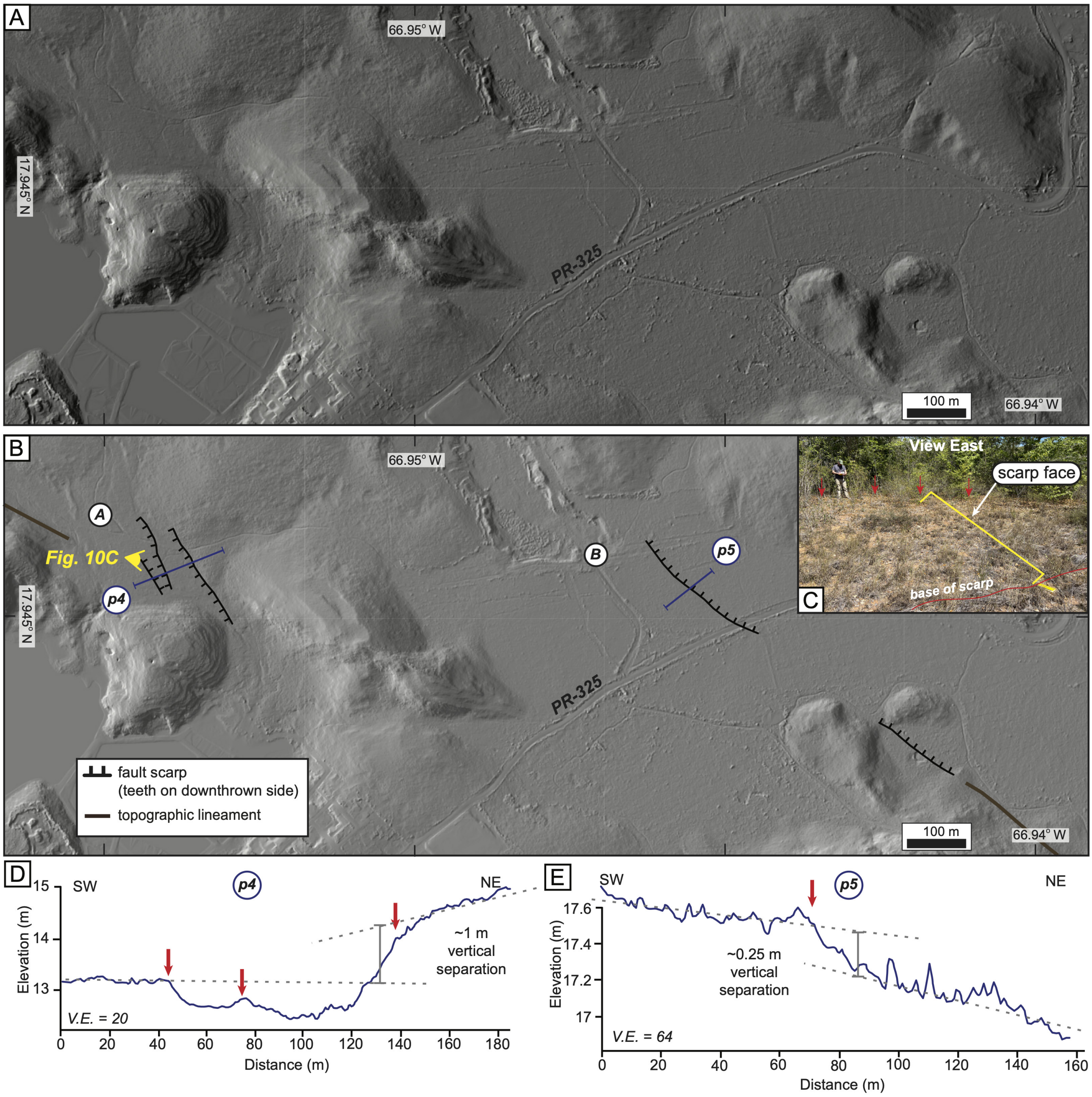

Figure 10 (A) Uninterpreted and (B) interpreted low-angle shaded relief map of the southeastern Punta Montalva fault derived from 1-m lidar data. Location in Figure 9. (C) Field photograph, looking northeast toward the scarp. Red arrows mark the top of the surface, red line marks the base of the scarp, and the face of the scarp is noted by yellow lines. Person for scale. (D) Topographic profile of three scarps across a small alluvial basin, recording ~1 m of total vertical separation, if surfaces are correlative. (E) Topographic profile of a scarp across a cultivated field, recording ~0.25 m of down-to-the-northeast (NE) vertical separation. Red arrow marks top of scarp mapped in the lidar-derived topography. SW —southwest; V.E.—vertical exaggeration.

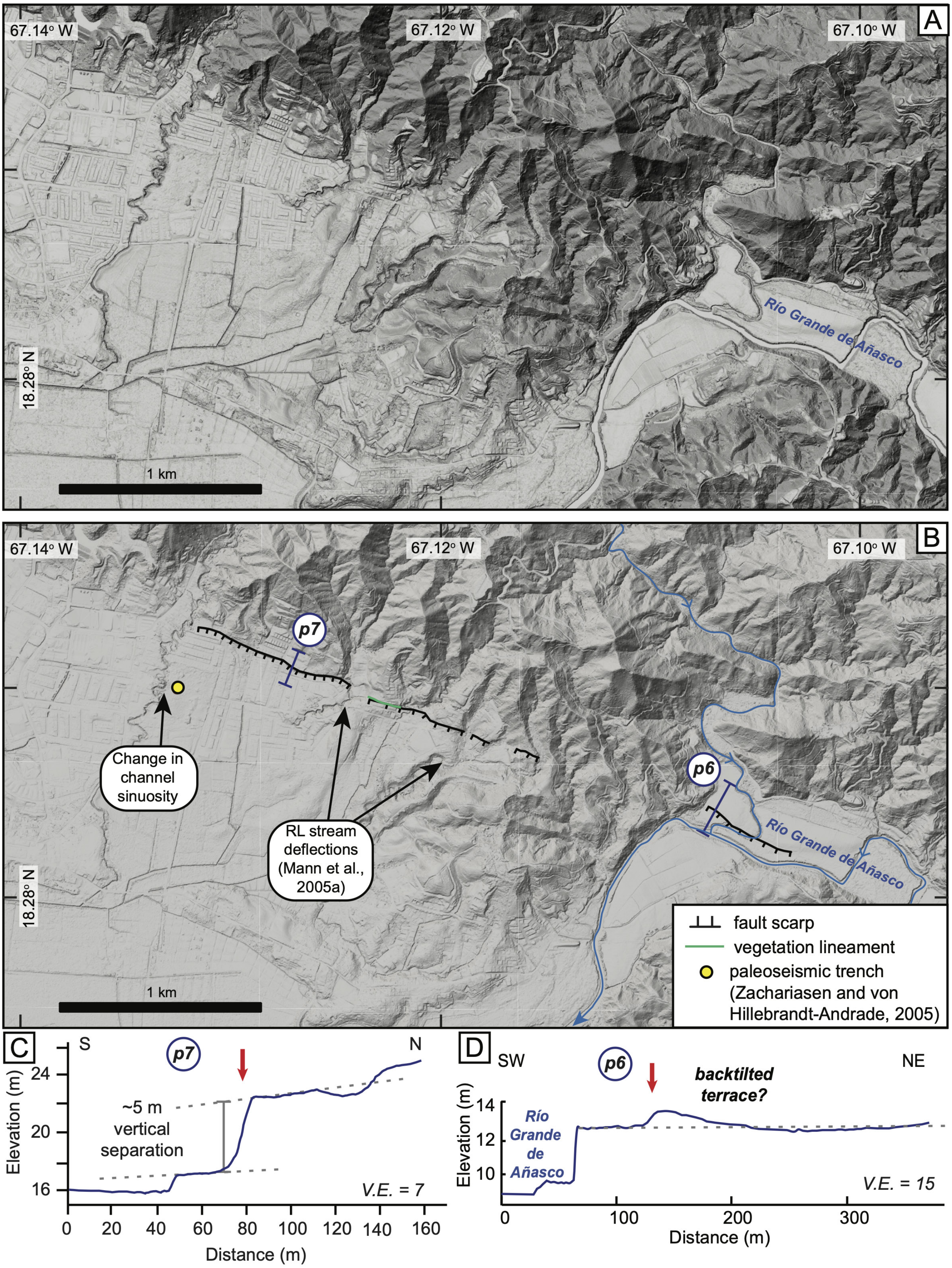

Figure 11 (A) Uninterpreted and (B) interpreted slope map of the eastern Cerro Goden fault derived from 1-m lidar data. Location in Figure 2. (C) Topographic profile of a possible backtilted terrace near the fault. (D) Topographic profile of a heavily modified scarp through a neighborhood, recording up to 5 m of down-to-the-south vertical separation. Red arrow marks top of scarp mapped in the lidar-derived topography. RL—right lateral; V.E.—vertical exaggeration.

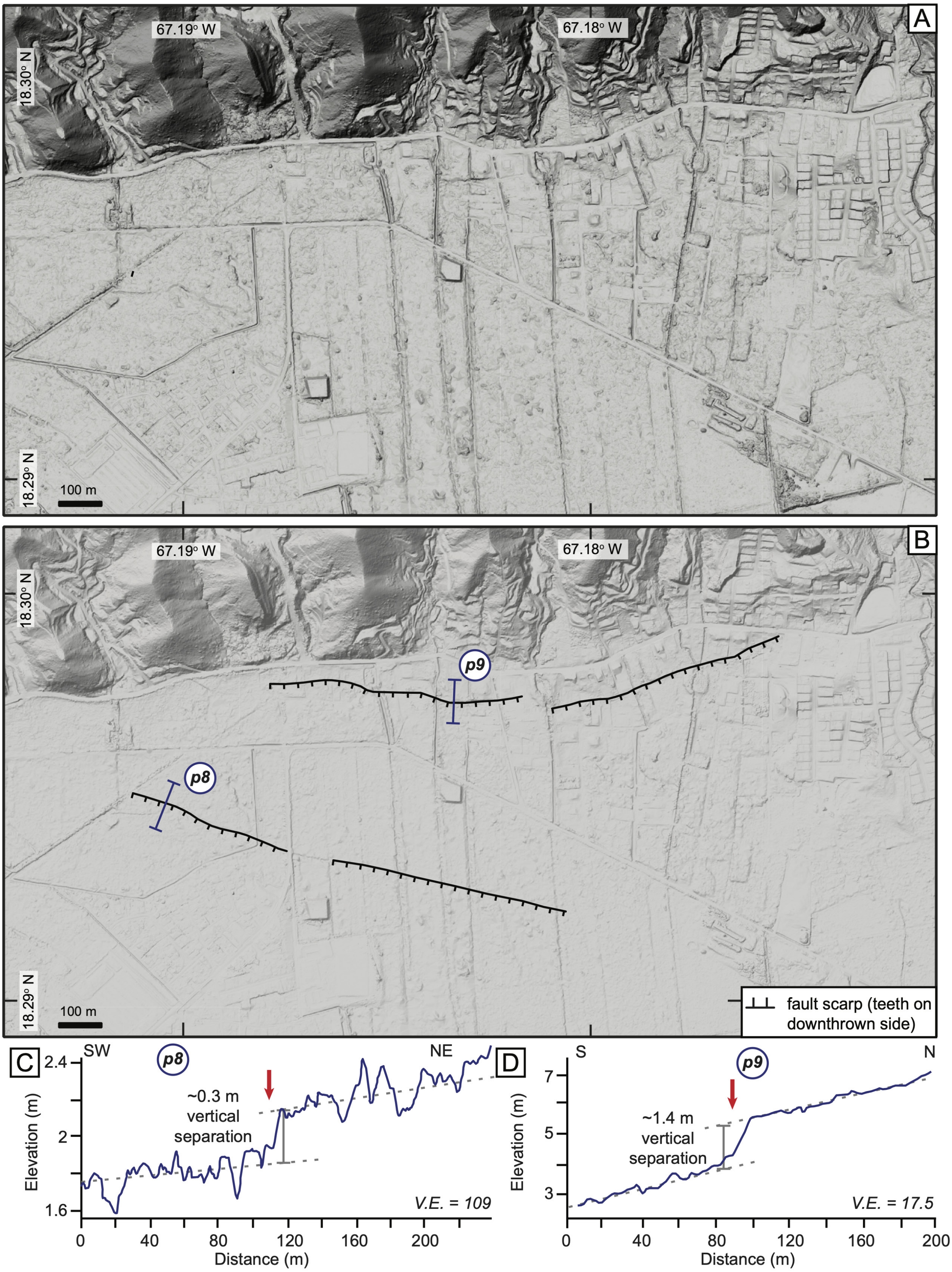

Figure 12 (A) Uninterpreted and (B) interpreted slope map of the western Cerro Goden fault derived from 1-m lidar data. Location in Figure 2. (C) Topographic profile from southwest (SW) to northeast (NE) of a subtle scarp recording ~0.3 m of down-to-the-south vertical separation. (D) Topographic profile from south (S) to north (N) of a modified scarp, recording up to 1.4 m of down-to-the-south vertical separation. Red arrow marks top of scarp mapped in the lidar-derived topography. V.E.—vertical exaggeration.

slip rate.

4.4 Salinas fault

The Salinas fault is located in southern Puerto Rico (Figure 1B), and generally trends east–west for ~22 km (Piety et al., 2018; Geomatrix Consultants, 1988). Glover (1971), based on unpublished gravity studies, mapped the Salinas fault as south-dipping with an $80°$ dip and normal (south down) kinematics. Geomatrix Consultants (1988) identified east–west and northwest–southeast-trending topographic scarps and lineaments, and using only estimated ages for alluvial surfaces, suggested that the fault has not ruptured in the Holocene but that late Quaternary (<35,000 yrs) rupture could have occurred. Subsequent mapping on lidar-derived topography and fault trenching (Piety et al., 2018) demonstrated that the Salinas fault is Holocene-active. Dated offset stratigraphy in a paleoseismic trench indicates at least two earthquakes: based on OSL ages, the penultimate earthquake occurred between 10.4 and 2.04 ka, and the most recent earthquake occurred between 2.66 and 2.04 ka (Piety et al., 2018). Based on conflicting ^{14}C ages, the penultimate earthquake occurred >14 ka and the most recent earthquake occurred 8–14 ka (Piety et al., 2018). Piety et al. (2018) also estimates a recurrence interval of ~4000 yrs based on OSL.

In the lidar-derived topography, prominent scarps and topographic lineaments trend east–west and are 300-m to 3.5-km long. Scarps are between 0.5–3.5-m-tall and face primarily south–southwest, with several north-facing scarps. Most of the fault zone has been well mapped by Piety et al. (2018) (Figure 13), but we mapped a few additional fault and fold scarps at the western end of the fault zone (Figure 14). The fold scarps have east-west orientations and are along strike of the mapped fault scarps in this study and Piety et al. (2018). On the lidar-derived topography, the fold scarps are expressed as broad warps that are 100–200-m wide, <1-m-tall, have an overall down-to-the-south displacement. The fold scarps can be seen as bends in the fabric of the agricultural fields. These fold scarps also coincide with changes in the channel planform of Río Inabón. Because of the uncertain origin of these fold scarps, we suggest they may represent a westward extension of the Salinas fault but further work would be beneficial to assess their origin and relationship to the mapped fault scarps to the east. We were unable to assess these fold scarps in the field.

In the field, at the western end of the Salinas fault zone near Fort Allen, scarps face south and are <1.2-m tall (Figure 15). The upper faulted surface appears to be heavily modified and may have been altered to serve as a canal system along the top edge of the scarps. Regardless, along strike within unmodified areas, the scarp persists with a similar magnitude of vertical offset as measured from the lidar-derived DEM. The scarps steps ~100 m to the south before continuing east with a similar orientation and vertical offset magnitude. Closer to the eastern end of the fault near the town of Salinas, scarps still face south but are slightly larger (<3-m tall).

We suggest the Salinas fault is at least 23- to 28-km long, with a primarily normal sense of movement, based on the presence of scarps, as well as tonal and topographic lineaments with a clear down-to-the-south displacement that are consistent with gravity data. Using scarps with vertical separations generally around 2 m and an assumed age of 10 ka for the offset geomorphic surfaces, we estimate a slip rate of ~0.2 mm/yr, consistent with estimates from Piety et al. (2018). Mismatches between stratigraphy across the fault within the paleoseismic trench (Piety et al., 2018) indicates a lateral component, and Piety et al. (2018) propose left-lateral movement based on a single apparently displaced channel. However, we interpret that within a kinematic framework, the fault is right-lateral to be consistent with the South Lajas fault along strike.

4.5 Great Southern Puerto Rico fault zone

The active Great Southern Puerto Rico fault zone (GSPRFZ) is located at the southeastern part of Puerto Rico and may span northwest to the northwestern coast near Aguadilla, trending N70W (Figure 1B). Because we do not observe evidence for young faulting in the mountains, our focus is on the southernmost extent of the GSPRFZ. Near the southern coast, the fault zone is ~2 km wide and has two main fault strands: the Río Jueyes and the Esmeralda faults (Piety et al., 2018). Near Central Aguirre, northwest-trending scarps that face both southwest and northeast cross alluvial deposits and can be mapped for a total distance of 8 km (Piety et al., 2018). A paleoseismic trench across the GSPRFZ revealed a 3-m-wide, $60-70°$ south-dipping fault zone (Piety et al., 2018). Offset units and scarp-derived colluvium in the trench document evidence for two surface ruptures, but earthquake timing remains unconstrained.

In the lidar-derived topography, scarps and topographic and tonal lineaments associated with the GSPRFZ generally strike west–northwest and vertically offset mapped Quaternary alluvial surfaces (Figures 16, 17), characterized as alluvial fans and piedmont alluvial gravels, likely of late Pleistocene to Holocene age (Berryhill Jr., 1960; Glover, 1961a,b). Scarps primarily face southwest but a few scarps face northeast, and range in length from 500 m to 1.8 km, for a total mapped fault zone length of ~17 km.

In the field, we observed scarps that range in height from <0.5 m to 2.5 m. At the southeastern end, a northeast-facing scarp has <2 m of vertical separation but is heavily modified, leading to large uncertainties on the scarp orientation and total vertical offset (Figure 16). This scarp aligns with a linear boundary in the bedrock to the northwest. To the west of the bedrock hills, a southwest-facing 1- to 2-m-tall scarp continues to the northwest across several agricultural fields (Figure 16). This scarp was trenched by Piety et al. (2018), who found evidence for one paleoearthquake with an inferred Holocene age. A few hundred meters to the northwest but offset by 200 m, tonal contrasts with approximately the same orientation trend northwest across several fields. At the northwestern end of the mapped scarps, directly north of the primary east–west highway along the southern coast (PR-52), we observed

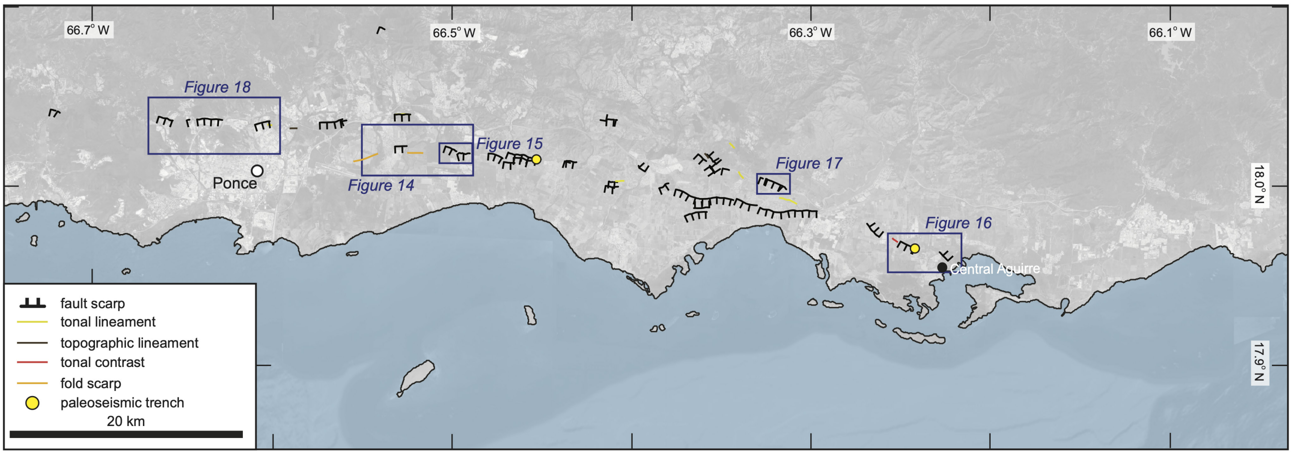

Figure 13 Overview of fault-related features mapped in southwestern Puerto Rico. Location shown on Figure 2. Paleoseismic trenches are from Piety et al. (2018). Background image is a blend of GoogleEarth imagery converted to grayscale overlain on a shaded relief map derived from the <1-m lidar data.

a 1-m-tall southwest-facing scarp that offsets Quaternary alluvial fans (Figure 17). Incised channels are possibly right-laterally offset or deflected by <10 m, indicating the fault likely accommodates oblique motion during the Quaternary.

The GSPRFZ has been documented in paleoseismic trenches (Piety et al., 2018) and has clear northeast- and southwest-facing scarps through mapped late Pleistocene and Holocene deposits in addition to tonal lineaments along strike at the same orientation. Based on these observations, we suggest at least the southeasternmost 17 km of the GSPRFZ is Holocene-active. Using an average vertical separation of ~2 m and an assumed 10 ka age of the deposits, the GSPRFZ has a vertical separation rate of 0.2 mm/yr. The fault likely has a lateral component based on orientations and facing directions of scarps, a mismatch in stratigraphy across the fault in the trench (Piety et al., 2018), and interpreted left-lateral offset of older bedrock units (Glover, 1971). Our observations would support right-lateral displacement, whereas older bedrock relationships indicate the fault accommodated left-lateral motion in the past (Glover, 1971). Regardless of the direction of lateral displacement, 0.2 mm/yr is likely a minimum fault slip rate.

4.6 San Marcos fault

The San Marcos fault is located in south-central Puerto Rico, and trends east–west (Figure 1B). The fault is best expressed as two prominent topographic scarps (Figure 18) in the El Madrigal area (Geomatrix Consultants, 1988). Krushensky and Monroe (1975, 1979) originally mapped the fault as a 3.8-km-long normal fault with down-to-the-south displacement in Oligocene bedrock. The eastern end of the fault is mapped as buried under alluvium from the Río Portugués, and the western end of the fault is truncated by a north-trending fault in the Río Cañas valley (Krushensky and Monroe, 1979). Geomatrix Consultants (1988) extend the fault farther east and west with a length of ~11 km based on photolineaments and field studies, but suggest the scarps observed in the field may be erosional fault-line scarps. However, they did observe that the fault displaced units estimated as Pliocene to early Pleistocene, but that the fault also likely has not ruptured in the last 35 ka. This interpretation was supported by terrace correlations which indicate the terraces upstream and downstream from the fault along the Río Portugués are not displaced (Geomatrix Consultants, 1988).

Development north of Ponce has obscured fault-related features in the lidar data; regardless, clear topographic steps are visible both in the lidar and field, represented by steps in the rows of houses. In the lidar-derived topography, scarps are between 150-m and 1.5-km long and are generally linear and along strike of each other, for a total length of ~16 km. Scarp heights vary from 0.4–7 m and are down-to-the-south. The scarps (Figure 18) can be traced across Quaternary alluvium and terraces interpreted to be Pleistocene and Holocene along the Río Pastillo, Río Cañas, and Río Portugués (Krushensky and Monroe, 1975, 1978) and have lower vertical displacements on apparently younger geomorphic surfaces (profile p14 in youngest terrace above modern river).

Future work would be beneficial to better document the fault trace and date deposits to determine slip rates and fault activity. We were unable to locate the outcrop described in Geomatrix Consultants (1988) that documents faulted Pliocene or early Pleistocene deposits for dating, but several other terrace surfaces may be potential future targets for geochronology.

4.7 Parguera fault

Along the southwestern coast, we mapped a series of east–west- and west-northwest–east-southeast-trending scarps and topographic and tonal lineaments (Figures 3, 19, 20). The scarps range in length from 200 m to 2.5 km. In the lidar-derived topography, the scarp heights range from 20 cm to 4 m, displacing alluvial fan surfaces.

We observed the scarps in alluvium at four different sites in the field. Where observed in the field, the scarp heights are commonly 20 cm up to 3.5 m, although heavy vegetation and extensive anthropogenic modifi-

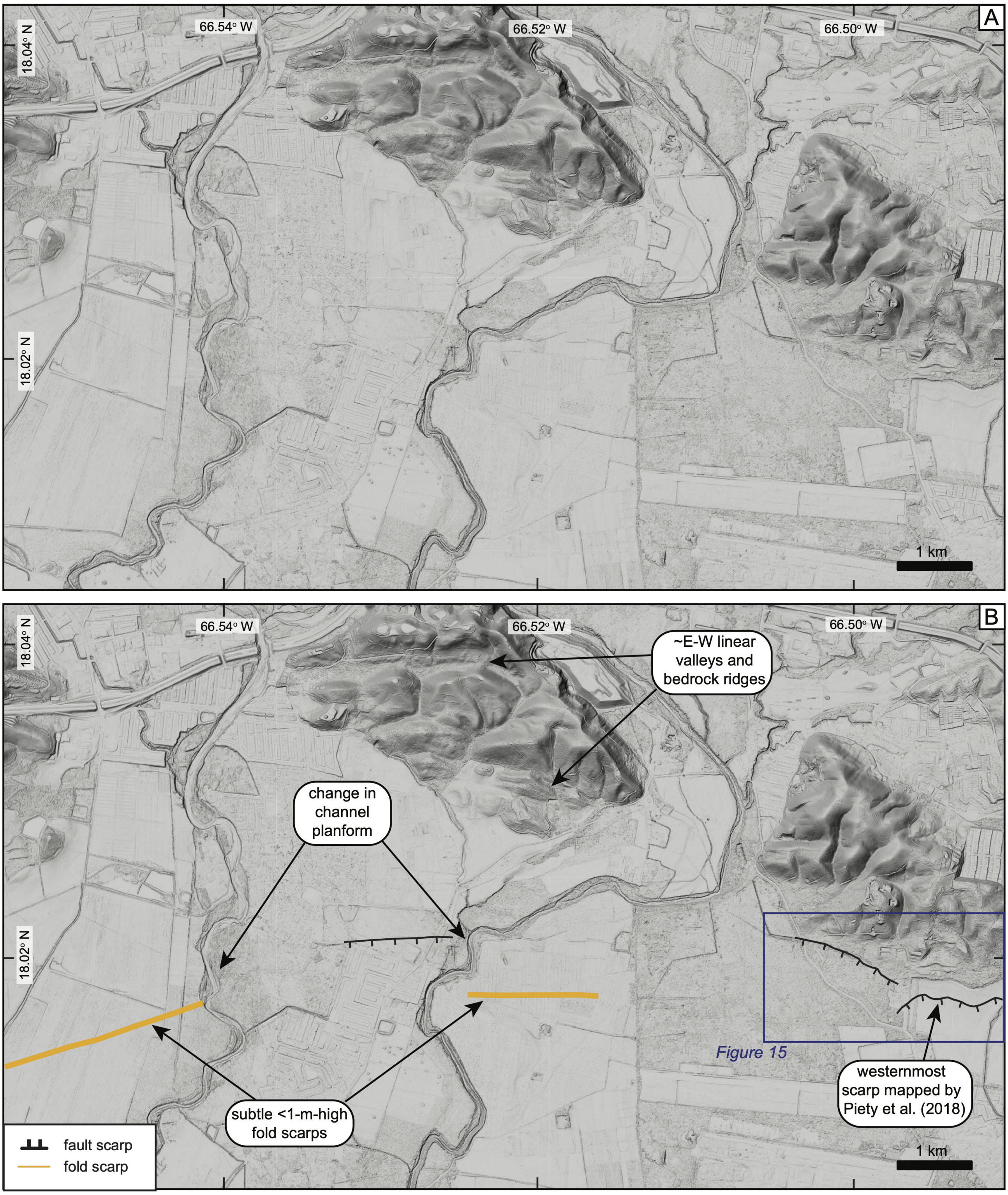

Figure 14 (A) Uninterpreted and (B) interpreted slope map of the western end of the Salinas fault derived from 1-m lidar data. Location in Figure 13. E-W—east-west.

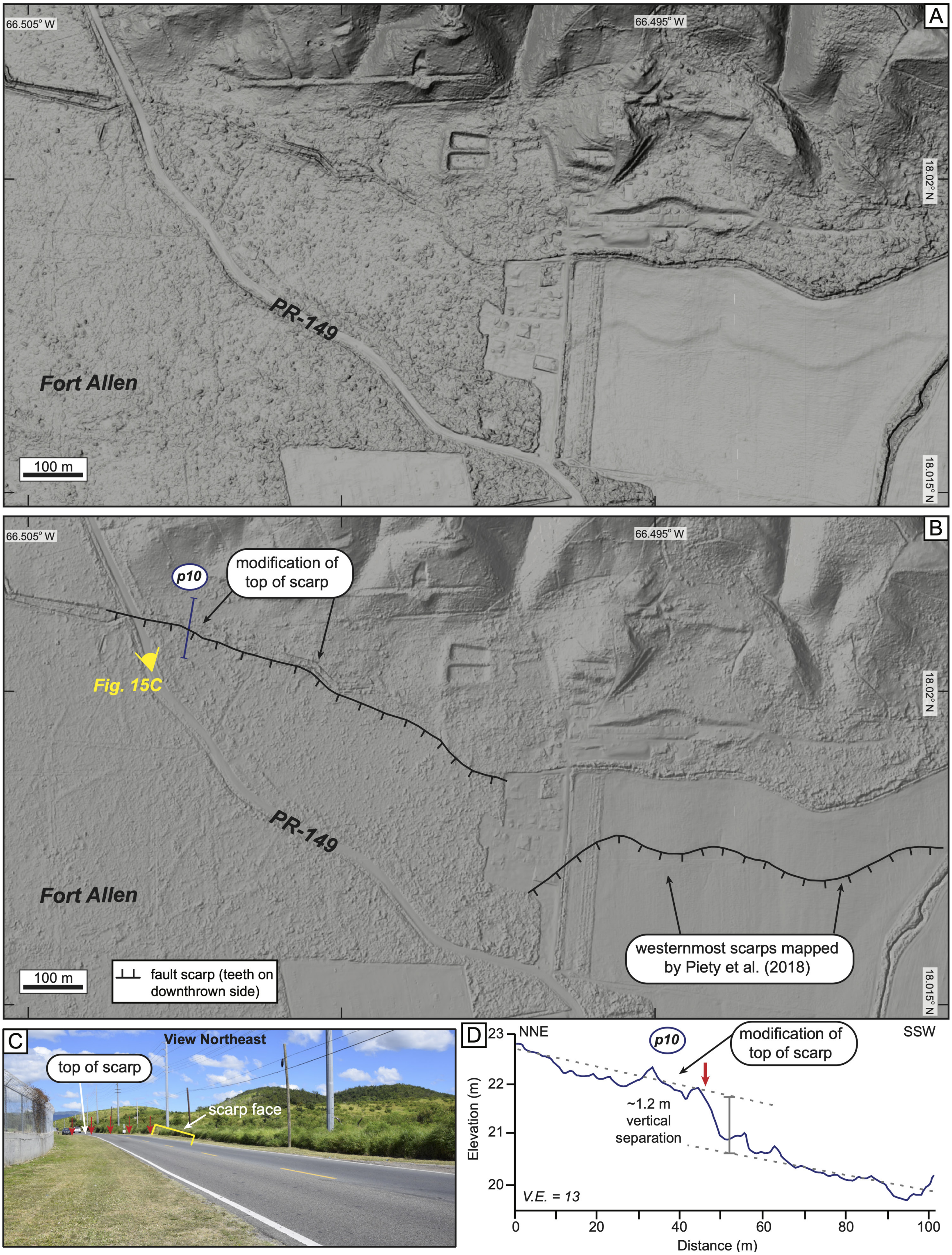

Figure 15 (A) Uninterpreted and (B) interpreted shaded relief map of the western Salinas fault derived from 1-m lidar data. Location in Figure 13 and 14. (C) Field photograph, looking north along the road that intersects the scarp. (D) Topographic profile from north-northeast (NNE) to south-southwest (SSW) of a modified scarp, recording ~1.2 m of down-to-the-south vertical separation. Red arrow marks top of scarp mapped in the lidar-derived topography. V.E.—vertical exaggeration.

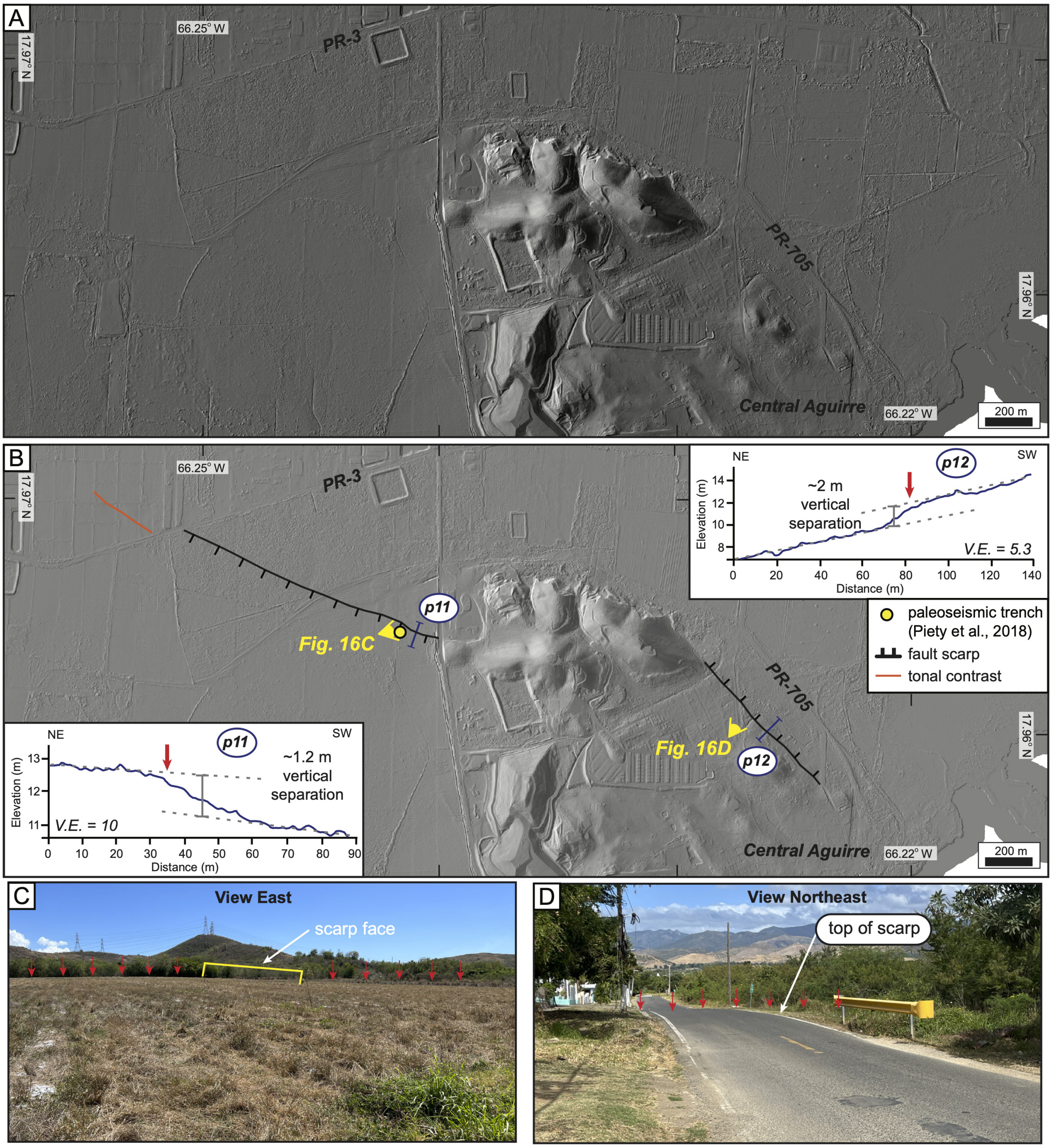

Figure 16 (A) Uninterpreted and (B) interpreted slope map of the Great Southern Puerto Rico fault zone derived from 1-m lidar data. Location in Figure 13. Insets show topographic profiles of two scarps, recording ~1 to 2 m of down-to-the-southwest and down-to-the-northeast vertical separation. In the insets, red arrows marks top of scarp mapped in the lidar-derived topography and V.E. stands for vertical exaggeration. (C) Field photograph of a 1.2-m-tall down-to-the-southwest scarp, trenched by Piety et al. (2018). Red arrows mark the top of the scarp. The photograph is looking at the scarp face, marked by the yellow lines. (D) Field photograph of a 2-m-tall down-to-the-northeast scarp. Red arrow marks top of scarp.

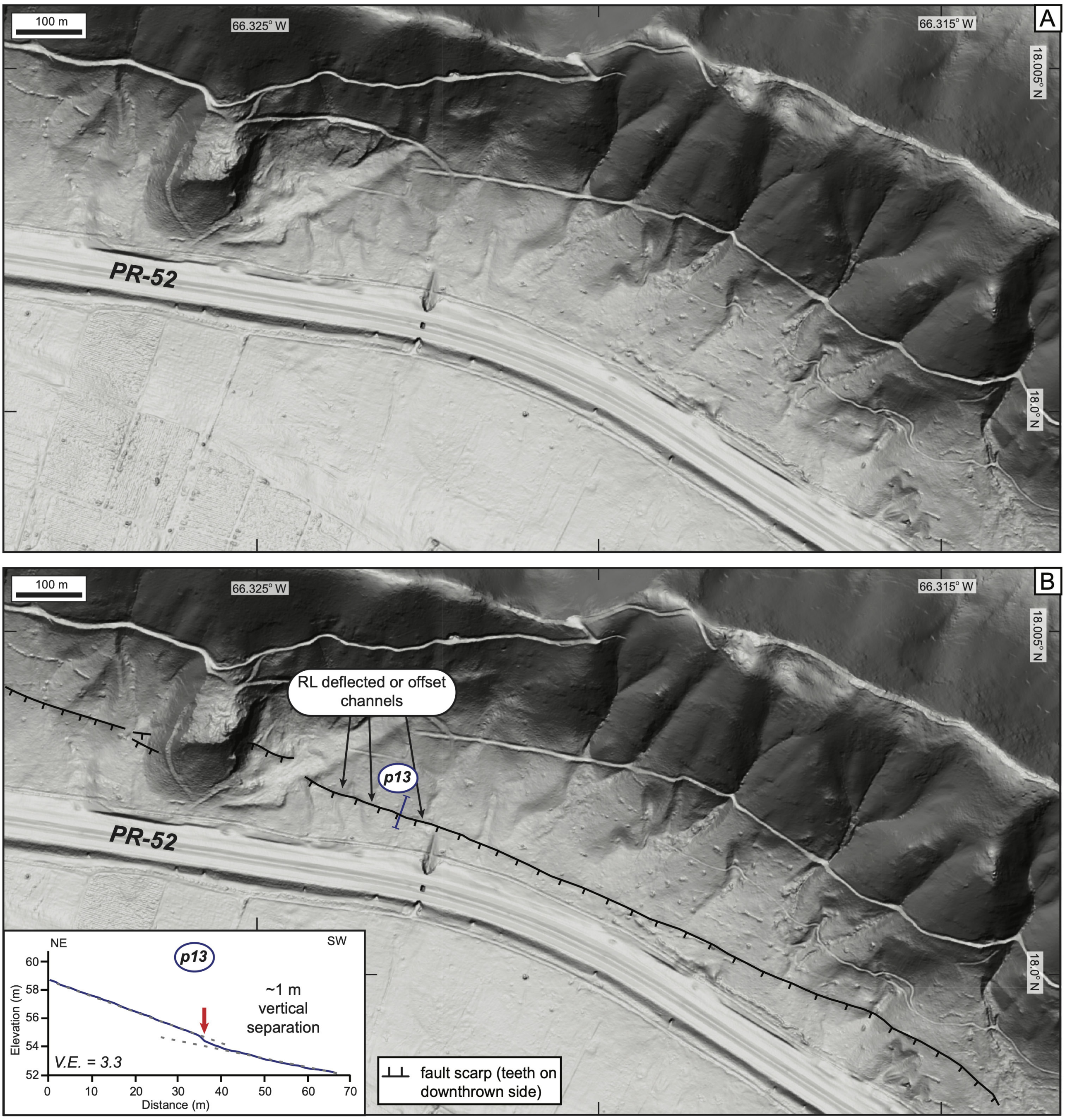

Figure 17 (A) Uninterpreted and (B) interpreted slope map of the Great Southern Puerto Rico fault zone derived from 1-m lidar data. Location in Figure 13. Inset shows topographic profile from northeast (NE) to southwest (SW) of a scarp, recording ~1 m of down-to-the-southwest vertical separation. Red arrow marks top of scarp mapped in the lidar-derived topography. RL—right lateral; V.E.—vertical exaggeration.

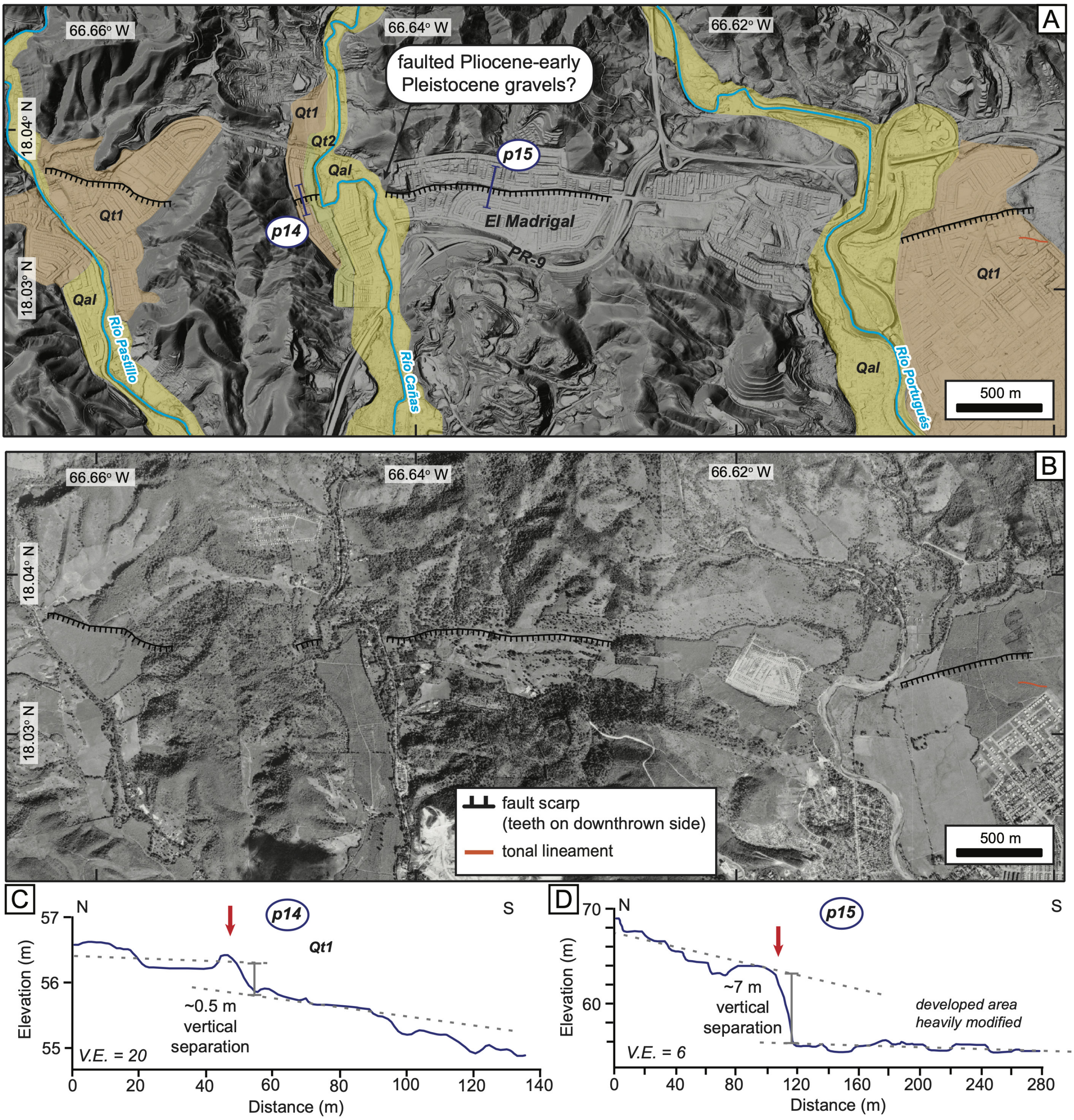

Figure 18 (A) Slope map derived from 1-m lidar data and (B) historical aerial imagery from 1962 of the San Marcos fault. Location in Figure 13. Location of faulted Pliocene-early Pleistocene gravels from Geomatrix Consultants (1988). (C) Topographic profile from north (N) to south (S) across a terrace of the Rio Cañas, recording possible <0.5-m-tall down-to-the-south scarp. (D) Topographic profile across the possible fault scarp in the El Madrigal neighborhood, which has been heavily modified, showing possible 5 to 7 m of down-to-the-south displacement. Geomorphic mapping modified from Krushensky and Monroe (1975) and Krushensky and Monroe (1978). Red arrow marks top of scarp mapped in the lidar-derived topography. V.E.—vertical exaggeration.

cation obscure the scarp at some locations. At one site, we observed a down-to-the-south scarp that vertically offsets an alluvial fan by 20-40 cm, but most sites record 1 to 2 m of vertical separation (Figures 19, 21). Near the western extent of the scarps in the town of La Parguera, a prominent step in the landscape is visible and can be traced west into an undeveloped region (Figure 20). However, because of dense vegetation, we were unable to verify scarp heights in the field. At the eastern end of La Parguera, a broad scarp face is visible crossing a field, and generally coincides with a mapped bedrock fault (Figure 21; Volckmann, 1984).

Despite the fact that these scarps parallel the coast, we do not interpret them to be related to sea-level change because (1) scarp heights vary and the scarp trace changes elevation along the coast; (2) the scarps clearly offset alluvial surfaces, and it is unlikely a relict coastline would be draped with alluvial material so uniformly; (3) along strike of the scarps, we observe topographic (saddles in ridges, linear ridges) and tonal lineaments; and (4) several lines of scarps coincide with mapped bedrock faults that are depicted as concealed under the Quaternary alluvium (Volckmann, 1984). Given that scarps exist in the Quaternary alluvium, we interpret that the faults may have been reactivated during the late Pleistocene or Holocene. Moreover, the presence of mangroves along the coast indicates possible subsidence of the region to the south of the scarps (Figures 19, 20), which agrees with the sense of motion observed on the scarps.

Therefore, we interpret these scarps to have a tectonic origin and represent late Pleistocene faulting along an east–west-trending fault, hereafter termed the Parguera fault. Future studies of the apparent scarps in the alluvium reported here would be beneficial to determine their origin and significance.

4.8 Great Northern Puerto Rico fault zone

The Great Northern Puerto Rico fault zone (GNPRFZ; Figure 1B) is a bedrock structure (M'Gonigle, 1978) defined by prominent topographic lineaments and linear range fronts. No definitive evidence for Holocene motion along the Cerro Mula fault of the GNPRFZ (Figure 1B); has been reported (Pase, 2007). Six paleoseismic trenches along different strands of the GNPRFZ have not yielded definitive evidence for late Pleistocene or Holocene rupture (Pase, 2007; Joyce, 2008; Williams Associates, 2008). One paleoseismic trench, the Peña Pobre East trench, records faulting of volcaniclastic units, but none of the fault strands extend upwards into the overlying younger alluvial units (Pase, 2007). Paleoliquefaction features were not found during a survey of rivers draining the northeast and east coasts (Tuttle, 2006), but were observed along the northern coast at the Río Grande de Manatí and may record up to three large ground-shaking events over the last 5,000 years (Figure 2; Tuttle et al., 2005). Although sedimentary conditions appear to be favorable along the Río Blanco, one of the main rivers draining the region of the Great Northern Puerto Rico fault zone, no paleoliquefaction features were observed (Figure 2; Tuttle, 2006; Pase, 2007).

In the lidar-derived topography, we identified several scarps and alignments of channel deflections that we could not definitively attribute to tectonic activity, although these features are near the inferred location of the Peña Pobre fault under Quaternary alluvium (Figure 22; M'Gonigle, 1978). Along the Río Peña Pobre, a 20- to 50-cm-tall south-facing scarp is visible across the lowest terrace. Across the river to the east, an alignment of northeast channel deflections near an 8- to 10-m-tall north-facing scarp is at a similar northeast orientation (Figure 22). These scarps are most likely fluvial terrace risers, because their orientations and sizes appear to most likely indicate a fluvial, rather than tectonic, origin. No scarps or other fault-related features were mapped on the lidar data farther east across the Río Blanco alluvial plain along the eastward continuation of the Peña Pobre fault trace, nor to the west near the Cerro Mula fault trace that was previously trenched (Pase, 2007).

The available data suggests the GNPRFZ has not hosted a major surface-rupturing earthquake in the late Pleistocene or Holocene; however, these observations do not preclude moderate events that may not have a preserved surface record. Moreover, the wetter climate and steeper terrain in this part of the island creates conditions that are less ideal for fault scarp preservation than in the southwestern part of the island.

4.9 San Francisco fault

The San Francisco fault trends east-west across the south-central part of Puerto Rico. In the landscape, the fault is expressed as prominent east-west linear valleys and ridges. Previous geologic mapping documents juxtaposed Cretaceous rocks against late Tertiary Ponce Limestone (Monroe, 1980). In addition, focal mechanisms from the 2019–ongoing seismic sequence indicate the San Francisco fault may have been reactivated during the sequence (ten Brink et al., 2022), although correlating seismicity with specific faults has remained ambiguous (e.g., Yoon et al., 2023). Mapping and observations from roadcuts and outcrops reveal evidence of possible recent faulting and definitively older faulting of Tertiary strata (Torres Angleró, 2021). However, the interpreted colluvial units remain undated. Our analysis of the lidar-derived topography did not definitively document any offset Quaternary deposits along the interpreted bedrock fault. Based on the existing geologic mapping (Grossman, 1963; Monroe, 1980; Torres Angleró, 2021) and our new remote mapping, we interpret that the San Francisco fault may not be active during the late Quaternary. Additional work to map Quaternary deposits along the fault in more detail would be helpful to assess if they could be faulted.

5 Discussion

5.1 Mapping context

Several factors may affect the mapped distribution of young faults we report here, including extensive anthropogenic modification, steep terrain with widespread

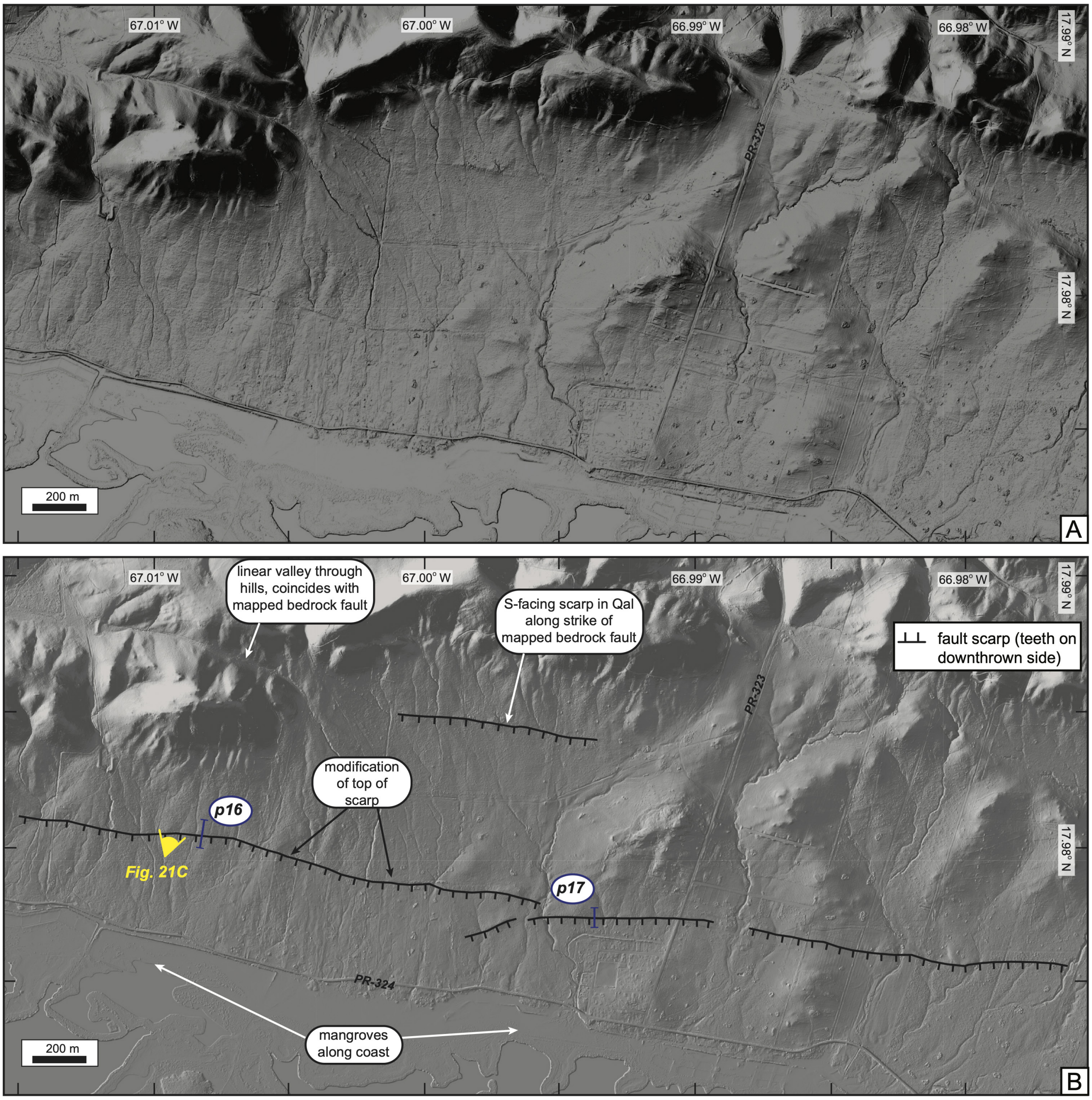

Figure 19 (A) Uninterpreted and (B) interpreted low-angle shaded relief map of the eastern extent of the Parguera fault zone derived from 1-m lidar data. Bedrock fault is mapped in Volckmann (1984). Location in Figure 3. S—south.

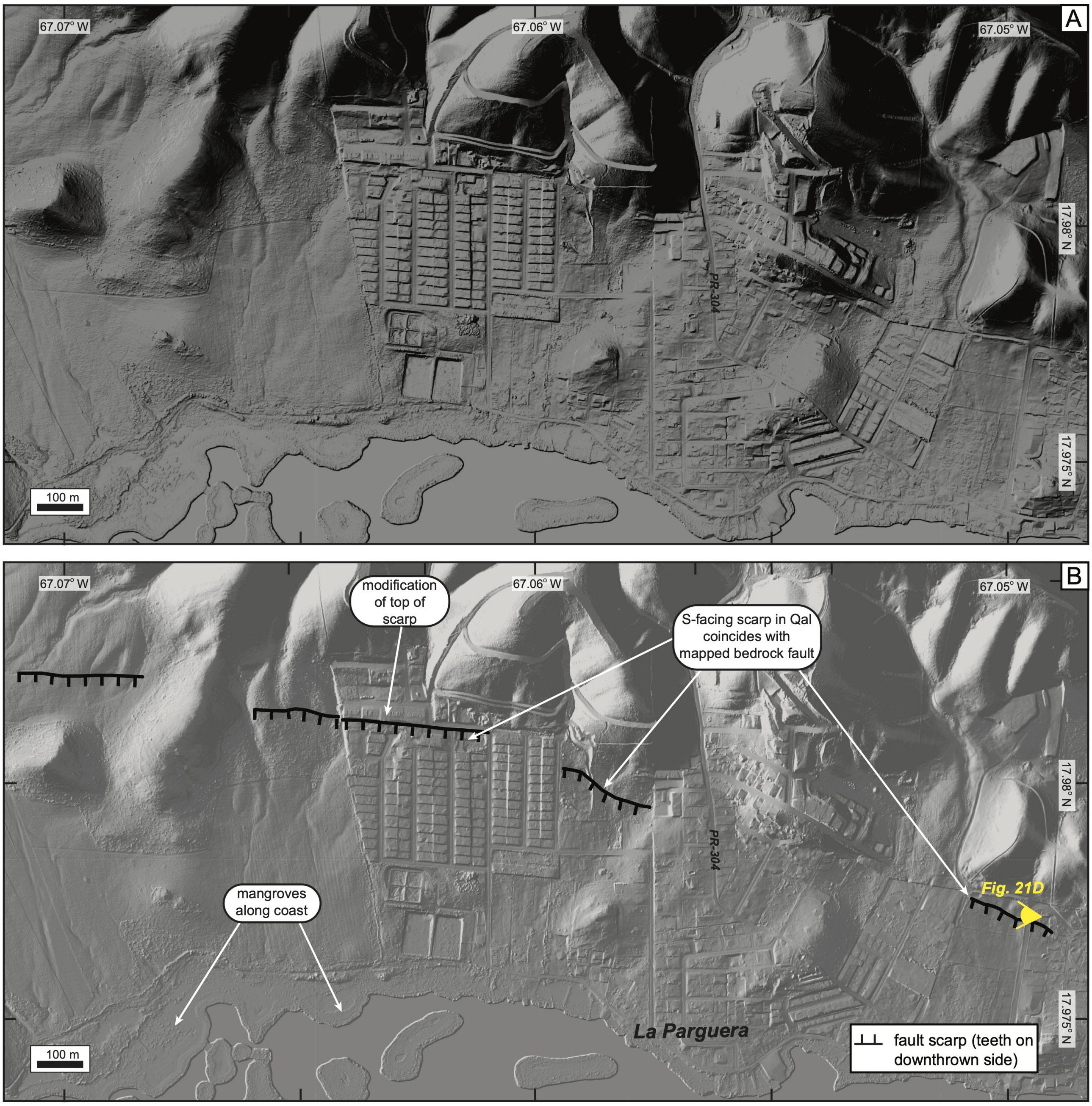

Figure 20 (A) Uninterpreted and (B) interpreted low-angle shaded relief map of the Parguera fault zone derived from 1-m lidar data. Mapped bedrock fault from Volckmann (1984). Location in Figure 3. S—south.

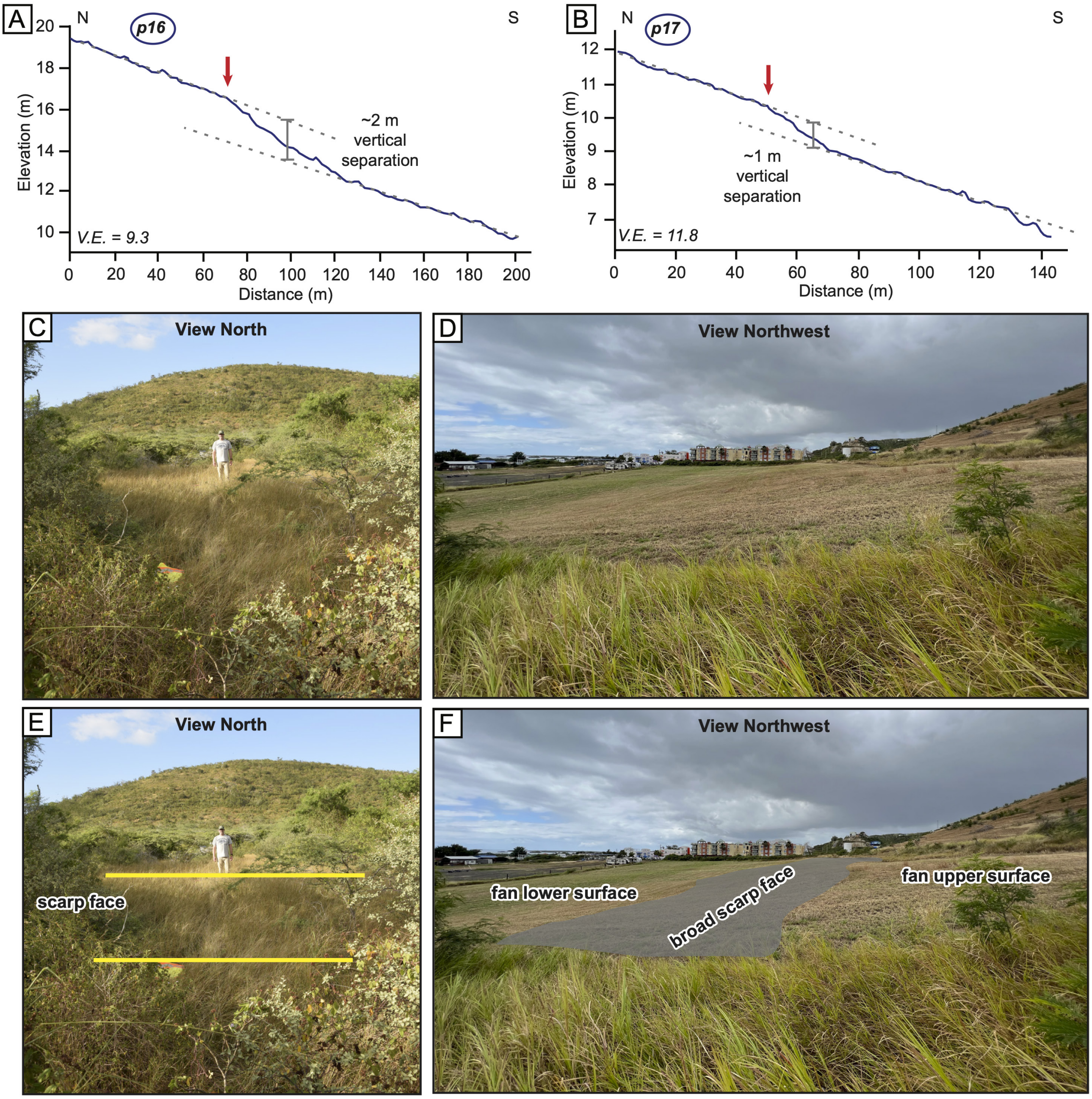

Figure 21 (A) and (B) topographic profiles from north (N) to south (S) showing 1 to 2 m of vertical separation across alluvial surfaces on the Parguera fault. Red arrow marks top of scarp mapped in the lidar-derived topography. V.E.—vertical exaggeration. Locations of profiles shown in Figure 19. (C) Uninterpreted and (E) interpreted field photograph showing the 2-m-tall scarp in the La Parguera Nature Reserve. Location of field photographs shown in Figure 19. (D) Uninterpreted and (F) interpreted field photograph showing a broad scarp face in a field at the east end of the town of La Parguera. This scarp broadly coincides with a mapped bedrock fault trace. Location of field photograph shown in Figure 20.

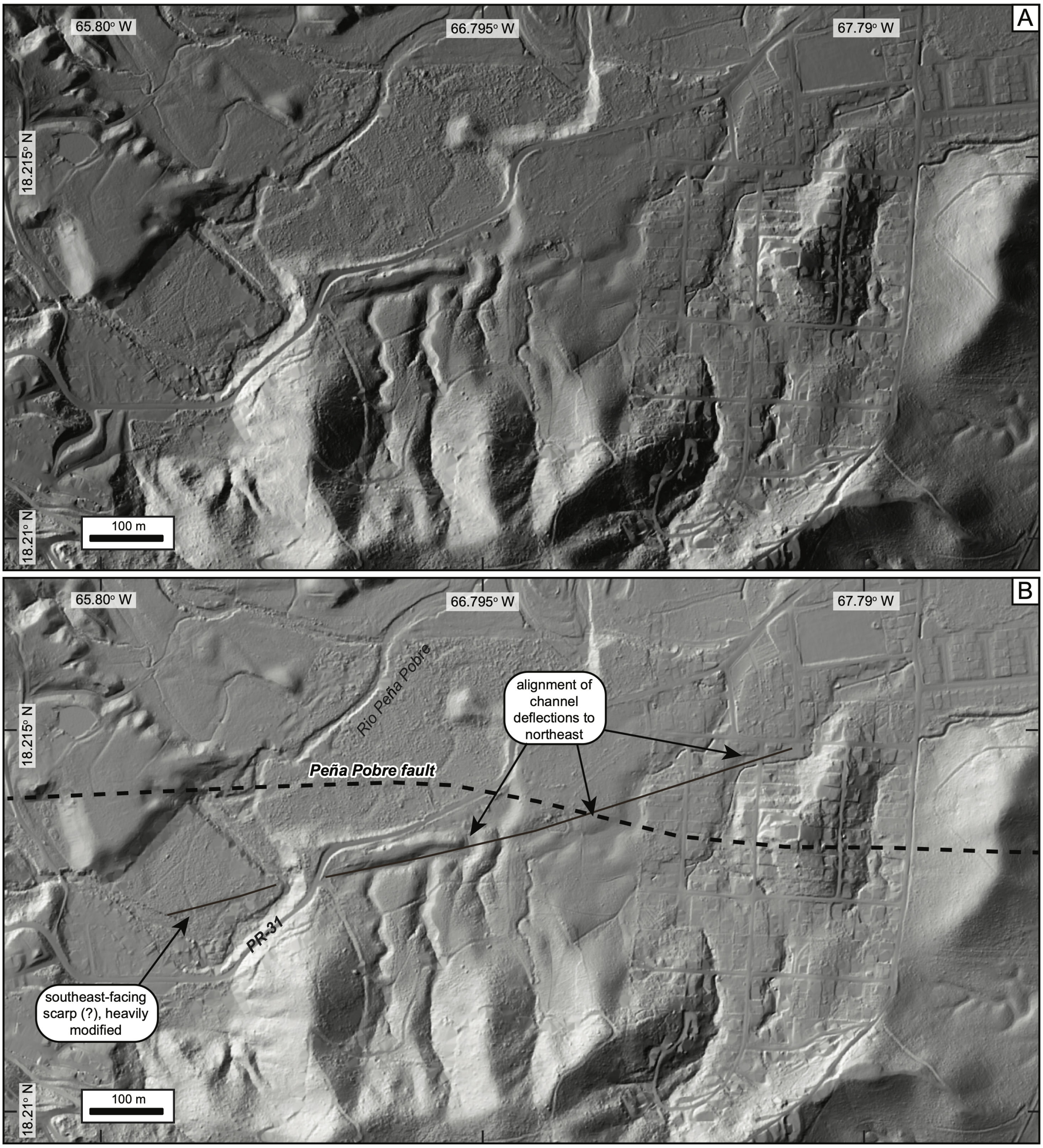

Figure 22 (A) Uninterpreted and (B) interpreted low-angle shaded relief map of the Peña Pobre area of the Great Northern Puerto Rico fault zone derived from <1-m lidar data. Approximate mapped trace of the Peña Pobre fault (dashed black line) under alluvium from M'Gonigle (1978). Brown line marks topographic lineament. Location in Figure 2.

landsliding, faults with slow (<1 mm/yr) slip rates, and strong bedrock expression in the landscape that may result in confusion between younger and older faulting. Most of the faults mapped in this study are located near the edges of the island, which is likely a consequence of the preservation of Quaternary deposits in the coastal and alluvial plains as well as the presence of river valleys wide enough to host flights of fluvial terraces. However, the perimeter of the island has also been culturally modified by agriculture and development, which may mask evidence of recent faulting. Within the interior of the island, the steep terrain coupled with landsliding may erase records of surface rupture.

Puerto Rico has a long-lived faulting history (Mann et al., 1995). Older faults and juxtapositions of different bedrock units create strong persistent lineaments across the landscape. These lineaments do not necessarily represent active faults. Moreover, the slow slip rates and long recurrence intervals (potentially several to tens of thousands of years) of many of the faults, derived from geodesy (e.g., Calais et al., 2016; Jansma et al., 2000) and field studies (e.g., Prentice and Mann, 2005; Piety et al., 2018), may result in the muted or absent geomorphic expression of active faults.

Despite these challenges and limitations, alluvial surfaces, especially along the southern coast, preserve clear evidence of active faulting. We cannot rule out that active faulting may continue into higher relief portions of the island (e.g., northwestern projection of the GSPRFZ). More work would be beneficial to test this idea because of the challenges described above.

5.2 Distribution of active faulting in Puerto Rico

Most of the Quaternary active faults we map coincide only generally with larger and older known fault zones. For example, the GSPRFZ only clearly displaces Quaternary deposits at its southeasternmost onshore extent, yet a much longer fault system that was active in the Cenozoic stretches northwest–southeast across the entire island (Glover, 1971; Hays, 1985). In another example, the scarps we map along the South Lajas fault zone do not align with the geomorphic rangefront along the valley margin. Instead, scarps along the South Lajas fault are generally basinward and in an echelon pattern removed up to several kilometers from the rangefront (Figure 5). One possible explanation for the apparent mismatch between recent and older faulting is that Quaternary faulting represents partial reactivation of existing faults, especially along the southern coast. Geodetic studies and the 2019–present seismic sequence show that deformation is focused along the southwestern corner of the island (Solares, 2019; ten Brink et al., 2022; Blasweiler et al., 2022; Yoon et al., 2023), and the modern strain field overprinted on older structures may account for the en echelon, discontinuous, and displaced map pattern of active faults and apparently different modern kinematics in comparison to older fault zones.

5.3 Updated Quaternary fault map for Puerto Rico

Following the precedent set in the Quaternary fault and fold database (QFFD), we classified faults based on the evidence for the presence and Quaternary activity of a fault (e.g., Crone and Wheeler, 2000; U.S. Geological Survey, 2023). Under this classification, Class A faults have strong geologic evidence for Quaternary activity of a fault with tectonic origin. Class B faults have weak or equivocal geologic evidence that demonstrates the existence of a Quaternary active fault, with a broad uncertainty in age constraints. Class C faults have insufficient geologic evidence to demonstrate either the existence of a tectonic fault or Quaternary deformation associated with the feature. Using this template, we classify the faults on Puerto Rico into 5 Class A faults, 3 Class B faults, and 2 Class C faults (Figure 23, Figure 24; Table 4).

In addition to assigning general confidence of Quaternary activity, we also assigned ranges of slip rates to faults with strong evidence for late Pleistocene and Holocene activity. We adopted ranges of slip rates slightly modified from those in the QFFD as follows: <0.5, 0.5–1, 1–5, and >5 mm/yr. The original QFFD slip rate bins are <0.2, 0.2–1, 1–5, and >5 mm/yr. A few studies report either slip rate or recurrence in Puerto Rico (e.g., Prentice and Mann, 2005; Piety et al., 2018); where known, we assigned a slip rate based on the available literature. Where slip rates were unknown, we estimated the rate based on geomorphic expression, vertical separation on scarps, and the age of the deposits. Commonly, we assumed a maximum Holocene age of 10 ka for young deposits near dated geomorphic surfaces (e.g., along the South Coast for the South Lajas, Salinas, Punta Montalva, and Great Southern Puerto Rico faults). For example, on the Salinas fault, using a vertical separation of 2 m and a maximum age of 10 ka for the surface, we estimate a vertical separation rate of 0.2 mm/yr. Given that many of these faults also include an unknown lateral component (e.g., South Lajas, Prentice and Mann, 2005; Salinas, Piety et al., 2018; Cerro Goden, Mann et al., 2005), if we assume equal amounts of vertical and lateral offset per event, this equates to an overall slip rate of ~0.3 mm/yr. Therefore, we would assign a slip rate range from 0 to 0.5 mm/yr to encompass uncertainties in the age, magnitude of vertical separation, and vertical to lateral slip ratio. All faults onshore Puerto Rico fall into this lowest categorical slip rate bin (0–0.5 mm/yr), consistent with the overall low geodetic rate (3 $\pm$2 mm/yr) measured across the island when summed (e.g., Jansma and Mattioli, 2005). We do not assign a slip rate bin to Class B and C faults.

5.4 Implications & Applications

Our lidar-based mapping and Quaternary active fault compilation confirms the presence of active faults that have been recognized in past studies (e.g., Piety et al., 2018; Styron et al., 2020), and we refine the locations and extents of these faults. We also report evidence for previously unrecognized scarps along the southern coast.

The faults mapped in this study were considered for

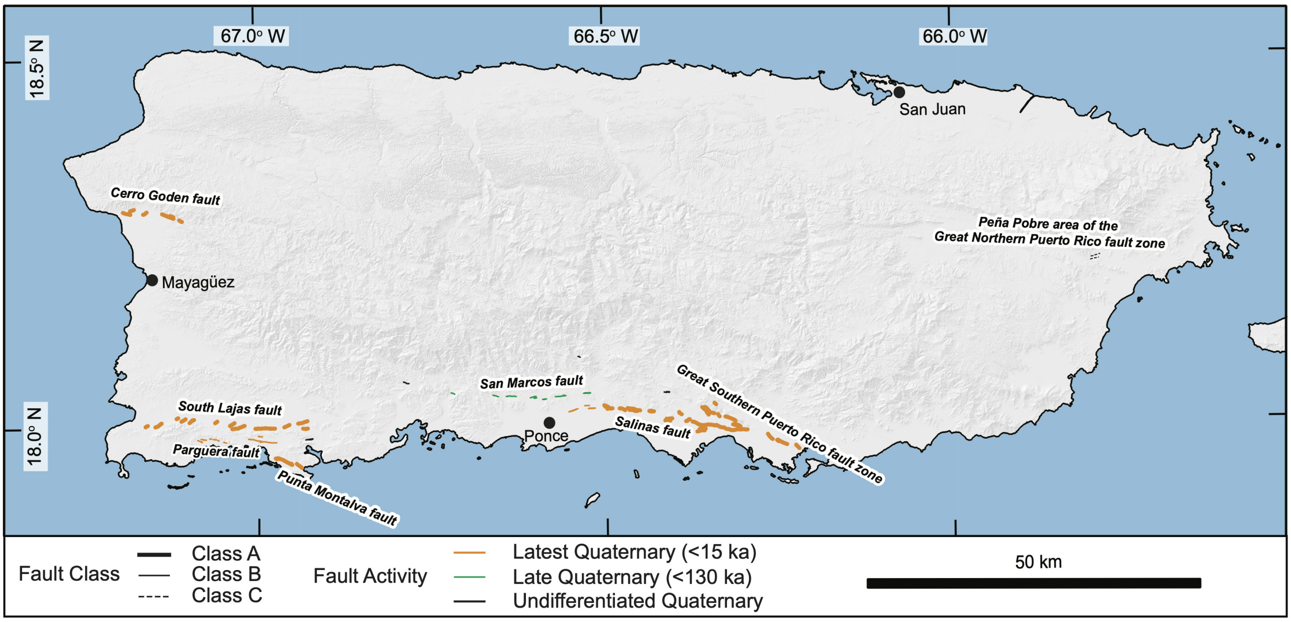

Figure 23 Quaternary fault map of onshore Puerto Rico, depicting traces of fault-related features, class (strength of geologic evidence for a Quaternary-active fault), and the timing of fault activity based on displaced dated deposits and geomorphic expression. The San Francisco fault is not shown because no fault-related features were mapped along the fault on the lidar-derived topographic data. Background image is a shaded relief map derived from the 10-m National Elevation Dataset digital elevation model (available at https://apps.nationalmap.gov/downloader/).

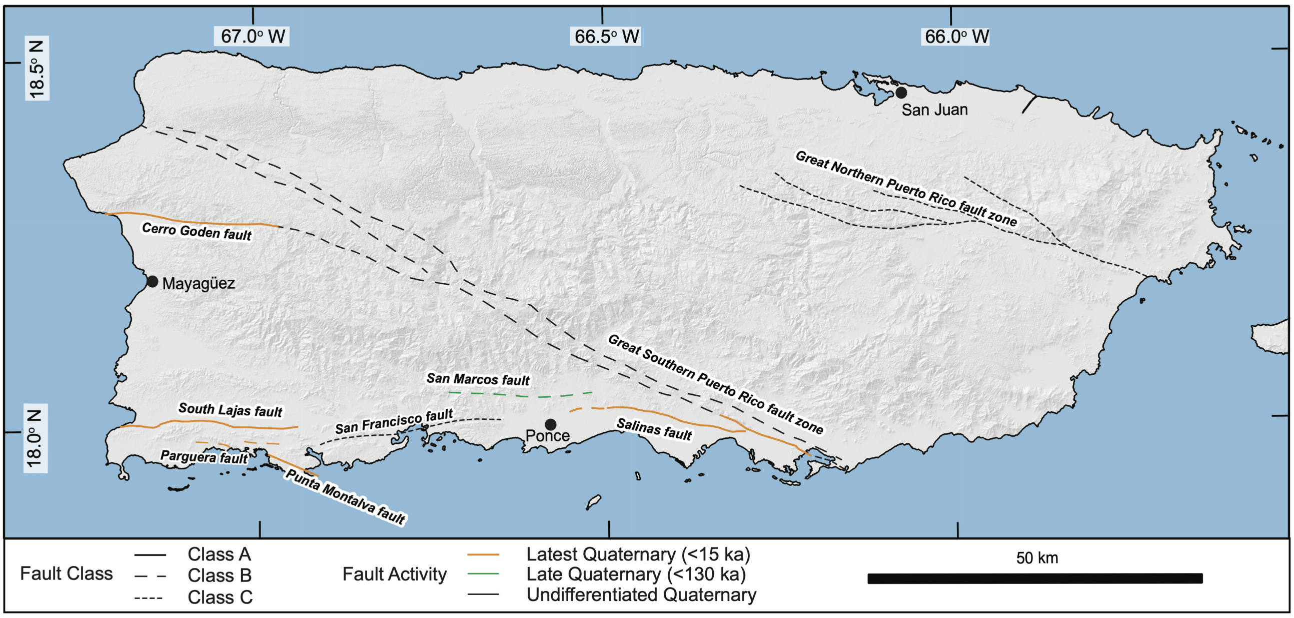

Figure 24 Simplified Quaternary fault map of onshore Puerto Rico, depicting simplified traces of fault-related features from this study and previous studies (Piety et al., 2018; Styron et al., 2020; Thompson Jobe et al., 2024b), class (strength of geologic evidence for a Quaternary-active fault), and the timing of fault activity based on displaced dated deposits and geomorphic expression. Background image is a shaded relief map derived from the 10-m National Elevation Dataset digital elevation model (available at https://apps.nationalmap.gov/downloader/).

Fault Name	Class	Age of Fault Activity	Categorical Slip Rate Bin (mm/yr)
South Lajas	A	Latest Quaternary (<15 ka)	0-0.5
Salinas	A	Latest Quaternary (<15 ka)	0-0.5
Great Southern Puerto Rico – southeast extent	A	Latest Quaternary (<15 ka)	0-0.5
Punta Montalva	A	Latest Quaternary (<15 ka)	0-0.5
Cerro Goden	A	Latest Quaternary (<15 ka)	0-0.5
Great Southern Puerto Rico – northwest extent	B	Undifferentiated Quaternary (<2.6 Ma)?	
Parguera	B	Latest Quaternary (<15 ka)?	
San Marcos	B	Late Quaternary (<130 ka)?	
Great Northern Puerto Rico	C		
San Francisco	C		

Table 4 Classification, age of fault activity, and categorical slip rate bins for onshore faults in Puerto Rico.

inclusion in the upcoming U.S. National Seismic Hazard Model (NSHM) 2025 update for Puerto Rico and the U.S. Virgin Islands if the evidence met NSHM criteria (Thompson Jobe et al., 2024b). Although mapped fault traces are generally discontinuous and en echelon (Figure 23), we interpret that they represent the surficial expression of the same seismogenic fault at depth (Figure 24), and in the context of the NSHM update, the complex surface traces we report here were greatly simplified (Thompson Jobe et al., 2024b).

Our mapping provides context for further active fault research, such as slip rate studies or assessments of earthquake histories from paleoseismic trenching (Figure 23). Additional studies on faults that transect the interior of the island are warranted to test the alternative hypotheses that modern deformation is focused along the western and southern coasts or that active faulting may cross the island.

6 Conclusion

We mapped fault-related features from 1-m lidar topography and historical aerial imagery across Puerto Rico to produce the foundation for an updated Quaternary fault map. We identified 134 features, most of which are scarps with heights between 0.5 and 3 m, that displace Quaternary deposits and that we interpret to represent the surface expression of tectonic faulting. We find that mapped active faults appear to reactivate only some older faults, and that modern faulting appears to be concentrated on the southern and western coasts of the island.

Acknowledgements

This work benefited from discussions with the U.S. Geological Survey (USGS) Puerto Rico-U.S. Virgin Islands Earthquake Geology working group, including Christopher DuRoss, Alex Hatem, Nadine Reitman, Thomas Pratt, Uri ten Brink, Sylvia Nicovich, Julie Herrick, and Camille Collett. Sierra Rack helped georeference historical aerial imagery. We thank two anonymous reviewers, USGS reviewer Sylvia Nicovich, and Editor Randy Williams for their constructive comments that improved this manuscript. This work was supported by the USGS Earthquake Hazards Program. Any use of trade, firm, or product names is for descriptive purposes only and does not imply endorsement by the U.S. Government.

Data Availability

Lidar data and 10-m National Elevation Dataset are available from The National Map at https://nationalmap.gov/. Geologic maps can be found at the National Geologic Map Database at https://ngmdb.usgs.gov/ and in the cited references. Earthquakes are from the USGS Advanced National Seismic System Comprehensive Catalog (ComCat) at https://earthquake.usgs.gov/data/comcat/ (U.S. Geological Survey, 2017). All data presented in this study (shapefiles of linework for fault-related features and simplified faults, structure-from-motion model of the Guanabanas road exposure of the South Lajas fault, radiocarbon, and OSL data) are available from Thompson Jobe et al. (2024a) and Mahan et al. (2024).

Competing interests

The authors have no competing interests.

References

Adames-Corraliza, A. Geomorphic and Geophysical Characterization of the North Boqueron Bay-Punta Montalva Fault Zone: A Capable Fault System in Southwestern Puerto Rico. M. s. thesis, University of Puerto Rico Mayagüez, 2017.

Berryhill Jr., H. L. Geology of the Central Aguirre quadrangle, Puerto Rico. Technical report, 1960. https://pubs.usgs.gov/publication/i318.

Blasweiler, M., Herman, M. W., Houtsma, F., and Govers, R. Tectonic context and possible triggering of the 2019–2020 Puerto Rico earthquake sequence. *Seismological Society of America*, 93 (2A):584–593, 2022. doi: 10.1785/0220210224.

Calais, E., Symithe, S., Mercier de Lépinay, B., and Prépetit, C. Plate boundary segmentation in the northeastern Caribbean from geodetic measurements and Neogene geological observations. *Comptes Rendus Geoscience*, 348(1):42–51, 2016. doi: 10.1016/j.crte.2015.10.007.

Crone, A. J. and Wheeler, R. L. Data for Quaternary faults, liquefaction features, and possible tectonic features in the Central and

Eastern United States, east of the Rocky Mountain Front. Technical report, 2000. https://pubs.usgs.gov/publication/ofr00260. Report.

Delano, J. E., Briggs, R. W., DuRoss, C. B., and Gold, R. D. Quick and Dirty (and Accurate) 3D Paleoseismic Trench Models Using Coded Scale Bars. *Seismological Research Letters*, 92(6): 3526–3537, May 2021. doi: 10.1785/0220200246.

DeMets, C., Jansma, P. E., Mattioli, G. S., Dixon, T. H., Farina, F., Bilham, R., Calais, E., and Mann, P. GPS geodetic constraints on Caribbean-North America Plate Motion. *Geophysical Research Letters*, 27(3):437–440, Feb. 2000. doi: 10.1029/1999gl005436.

Dolan, J. F. and Wald, D. J. The 1943-1953 North-Central Caribbean Earthquakes: Active Tectonic Setting, Seismic Hazards, and Implications for Caribbean-North America Plate Motions. *Special Paper-Geological Society of America*, (326):143–169, 1998.

Dolan, J. F., Mullins, H. T., and Wald, D. J. Active tectonics of the north-central Caribbean: Oblique collision, strain partitioning, and opposing subducted slabs. In *Active Strike-Slip and Collisional Tectonics of the Northern Caribbean Plate Boundary Zone*. Geological Society of America, 01 1998. doi: 10.1130/0-8137-2326-4.1.

Durcan, J. A., King, G. E., and Duller, G. A. DRAC: Dose Rate and Age Calculator for trapped charge dating. *Quaternary Geochronology*, 28:54–61, June 2015. doi: 10.1016/j.quageo.2015.03.012.

DuRoss, C. B., Gold, R. D., Dawson, T. E., Scharer, K. M., Kendrick, K. J., Akciz, S. O., Angster, S. J., Bachhuber, J., Bacon, S., Bennett, S. E., et al. Surface displacement distributions for the July 2019 Ridgecrest, California, earthquake ruptures. *Bulletin of the Seismological Society of America*, 110(4):1400–1418, 2020. doi: 10.1785/0120200058.

Galbraith, R. F., Roberts, R. G., Laslett, G. M., Yoshida, H., and Olley, J. M. Optical dating of single and multiple grains of quartz from Jinmium rock shelter, northern Australia: Part I, experimental design and statistical models. *Archaeometry*, 41(2):339–364, Aug. 1999. doi: 10.1111/j.1475-4754.1999.tb00987.x.

Galíndez, I. M. B. Evaluation of Geomorphic Proxies from High Resolution Topographic Dems in Oblique Subduction Zones: Western Puerto Rico. M. s. thesis, Oklahoma State University, 2018.

Geomatrix Consultants. Geological–seismological evaluation to assess potential earthquake ground motions for the Portugues Dam, Puerto Rico. Technical report, 1988. Report completed under Contract No. DAWC17-88-C-0003, submitted to Department of the Army, Jacksonville District, Corps of Engineers, Jacksonville, Florida, Project1311A.

Gile, L. H., Peterson, F. F., and Grossman, R. B. Morphological and genetic sequences of carbonate accumulation in desert soils. *Soil Science*, 101(5):347–360, 1966.

Glover, L. Preliminary geologic map of the Salinas Quadrangle, Puerto Rico, U.S. *Geological Survey Miscellaneous Investigations Map IMAP 337*, scale 1:20,000, 1961a. doi: 10.3133/i337.

Glover, L. Preliminary geologic map of the Coama Quadrangle, Puerto Rico, U.S. *Geological Survey Miscellaneous Investigations Map IMAP 335*, scale 1:20,000, 1961b. doi: 10.3133/i335.

Glover, L. Geology of the Coamo area, Puerto Rico, and its relation to the volcanic arc-trench association. *US Geological Survey Professional Paper 636*, page 102, 1971. doi: 10.3133/pp636.

Grindlay, N. R., Abrams, L. J., Del Greco, L., and Mann, P. Toward an integrated understanding of Holocene fault activity in western Puerto Rico: Constraints from high-resolution seismic and sidescan sonar data. In *Active Tectonics and Seismic Hazards of Puerto Rico, the Virgin Islands, and Offshore Areas*. Geological Society of America, 01 2005. doi: 10.1130/0-8137-2385-X.139.

Grossman, I. Geology of the Guanica-Guayanilla Bay area, southwestern Puerto Rico. *Geological Survey Research*, 1963.

Hays, W. Fundamentals of geology and regional geology for solving earthquake engineering problems in the Puerto Rico area. *USGS Open-File Report*, pages 85–731, 1985.

Hubbard, D. K., Gill, I. P., Burke, R. B., and Morelock, J. Holocene reef backstepping—southwestern Puerto Rico shelf. In *Proc 8th Int Coral Reef Symp*, volume 2, pages 1779–1784, 1997.

Jansma, P. E. and Mattioli, G. S. GPS results from Puerto Rico and the Virgin Islands: Constraints on tectonic setting and rates of active faulting. In *Active Tectonics and Seismic Hazards of Puerto Rico, the Virgin Islands, and Offshore Areas*. Geological Society of America, 01 2005. doi: 10.1130/0-8137-2385-X.13.

Jansma, P. E., Mattioli, G. S., Lopez, A., DeMets, C., Dixon, T. H., Mann, P., and Calais, E. Neotectonics of Puerto Rico and the Virgin Islands, northeastern Caribbean, from GPS geodesy. *Tectonics*, 19(6):1021–1037, Dec. 2000. doi: 10.1029/1999tc001170.

Joyce, J. Rio Valenciano Dam project, Bedrock fault structural analysis, Appendix F in Luis O. Garcia Associates, Seismic hazard analysis, Rio Valenciano dam site. Technical report, 2008. Juncos, Puerto Rico, Project No. 3557-06, Report prepared for GSA Group Architects and Engineers, San Juan, Puerto Rico, on behalf of The Puerto Rico Aqueduct and Sewer Authority.

Krushensky, R. and Monroe, W. Geologic map of the Ponce Quadrangles, Puerto Rico. *U.S. Geological Survey Miscellaneous Investigations Map IMAP 863*, scale 1:20,000, 1975. doi: 10.3133/i1863.

Krushensky, R. and Monroe, W. Geologic map of the Penuelas and Punta Cuchara Quadrangles, Puerto Rico. *U.S. Geological Survey Miscellaneous Investigations Map IMAP 1042*, scale 1:20,000, 1978. doi: 10.3133/i1042.

Krushensky, R. and Monroe, W. Geologic map of the Yauco and Punta Verraco Quadrangles, Puerto Rico. *U.S. Geological Survey Miscellaneous Investigations Map IMAP 1147*, 1979. doi: 10.3133/i1147.

López Marrero, T., Lorenzo Pérez, M., Rivera López, C., González Toro, A., Rivera Santiago, D., Nieves Crespo, H., and Hernandez González, P. Porto Rico 1930 Georeferenced: A Coastal Mosaic. In *Interdisciplinary Center for Coastal Studies*. University of Puerto Rico, Mayaguez, PR, 2017. Mayagüez Campus. 15 p. Available at https://prgeoref.weebly.com/1930-y-1936.html.

Mahan, S., Gray, H., and Jobe, J. Data release for Luminescence: Neotectonic mapping of Puerto Rico, 2024. https://doi.org/10.5066/P9EAILCD.

Mann, P., Taylor, F., Edwards, R., and Ku, T.-L. Actively evolving microplate formation by oblique collision and sideways motion along strike-slip faults: An example from the northeastern Caribbean plate margin. *Tectonophysics*, 246(1–3):1–69, June 1995. doi: 10.1016/0040-1951(94)00268-e.

Mann, P., Prentice, C. S., Hippolyte, J.-C., Grindlay, N. R., Abrams, L. J., and Laó-Dávila, D. Reconnaissance study of Late Quaternary faulting along Cerro Goden fault zone, western Puerto Rico. In *Active Tectonics and Seismic Hazards of Puerto Rico, the Virgin Islands, and Offshore Areas*. Geological Society of America, 01 2005. doi: 10.1130/0-8137-2385-X.115.

McCann, W. and Pannington, W. Seismicity, large earthquakes, and the margin of the Caribbean plate. *The geology of North America*, l:291–306,, 1990. doi: 10.1130/DNAG-GNA-H.291.

McCann, W., Feldman, L., and McCann, M. Catalog of felt earthquakes for Puerto Rico and neighboring islands 1493-1899 with additional information for some 20th century earthquakes. *Revista Geofísica*, 62:141–220, 2010.

McIntyre, D. Geologic map of the Central La Plata Quadrangle, Puerto Rico. *U.S. Geological Survey Miscellaneous Investigations Map IMAP 660*, scale 1:20,000, 1971. doi: 10.3133/i660.

Monroe, W. H. Geology of the middle Tertiary formations of Puerto Rico. *US Geological Survey Professional Paper 953*, 1980. doi: 10.3133/pp953.

Morelock, J., Winget, E. A., and Goenaga, C. Geologic maps of the southwestern Puerto Rico Parguera to Guanica insular shelf. *U.S. Geological Survey Miscellaneous Investigations Map IMAP 2387*, scale 1:40,000, 1994. doi: 10.3133/i2387.

M'Gonigle, J. Geologic map of the Humacao Quadrangle, Puerto Rico. *U.S. Geological Survey Miscellaneous Investigations Map IMAP 1070*, scale 1:20,000, 1978. doi: 10.3133/i1070.

Pacheco, J. F. and Sykes, L. R. Seismic moment catalog of large shallow earthquakes, 1900 to 1989. *Bulletin of the Seismological Society of America*, 82(3):1306–1349, June 1992. doi: 10.1785/bssa0820031306.

Pase, D. Tectonic activity of the Great Northern Puerto Rico fault zone—A remote sensing interpretation and field validation study. M. s. thesis, University of Memphis, Tennessee, 2007.

Piety, L. A., Redwine, J. R., Derouin, S. A., Prentice, C. S., Kelson, K. I., Klinger, R. E., and Mahan, S. Holocene Surface Ruptures on the Salinas Fault and Southeastern Great Southern Puerto Rico Fault Zone, South Coastal Plain of Puerto Rico. *Bulletin of the Seismological Society of America*, 108(2):619–638, Jan. 2018. doi: 10.1785/0120170182.

Prentice, C. S. and Mann, P. Paleoseismic study of the South Lajas fault: First documentation of an onshore Holocene fault in Puerto Rico. In *Active Tectonics and Seismic Hazards of Puerto Rico, the Virgin Islands, and Offshore Areas*. Geological Society of America, Jan. 2005. doi: 10.1130/0-8137-2385-X.215.

Reid, H. F. and Taber, S. The Porto Rico Earthquakes of October-November, 1918. *Bulletin of the Seismological Society of America*, 9(4):95–127, Dec. 1919. doi: 10.1785/bssa0090040095.

Reitman, N. G., Bennett, S. E. K., Gold, R. D., Briggs, R. W., and DuRoss, C. B. High-Resolution Trench Photomosaics from Image-Based Modeling: Workflow and Error Analysis. *Bulletin of the Seismological Society of America*, 105(5):2354–2366, Sept. 2015. doi: 10.1785/0120150041.

Ríos, R. V., Comas, L. M., Sturm, P., and Ferguson, R. Lajas Valley Agricultural Reserve farm inventory of the Guánica Lagoon, El Anegado and adjacent areas Guánica, Puerto Rico, 2012. https://repository.library.noaa.gov/view/noaa/830. Professional Paper.

Roig-Silva, C. M. Geology and structure of the north Boqueron Bay-Punta Montalva fault system. M. s. thesis, University of Puerto Rico Mayagüez, 2010.

Roig-Silva, C. M., Asencio, E., and Joyce, J. The Northwest Trending North Boqueron Bay-Punta Montalva Fault Zone; A Through Going Active Fault System in Southwestern Puerto Rico. *Seismological Research Letters*, 84(3):538–550, May 2013. doi: 10.1785/0220120115.

Schoeneberger, P., Wysocki, D., Benham, E., and Staff, S. S. Field book for describing and sampling soils, Version 3.0. *Natural Resources Conservation Service, National Soil Survey Center*, page 298, 2012.

Solares, M. New constraints on crustal deformation within the Puerto Rico-Virgin Islands Microplate using two decades of GPS data. M. s. thesis, University of Puerto Rico Mayagüez, 2019.

Styron, R., García-Pelaez, J., and Pagani, M. CCAF-DB: the Caribbean and Central American active fault database. *Natural Hazards and Earth System Sciences*, 20(3):831–857, Mar. 2020. doi: 10.5194/nhess-20-831-2020.

ten Brink, U. S., Bakun, W. H., and Flores, C. H. Historical perspective on seismic hazard to Hispaniola and the northeast Caribbean region. *Journal of Geophysical Research: Solid Earth*, 116(B12), 2011. doi: https://doi.org/10.1029/2011JB008497.

ten Brink, U. S., Vanacore, E., Fielding, E. J., Chaytor, J. D., López-Venegas, A. M., Baldwin, W. E., Foster, D. S., and Andrews, B. D. Mature diffuse tectonic block boundary revealed by the 2020 southwestern Puerto Rico seismic sequence. *Tectonics*, 41(3): e2021TC006896, 2022. doi: 10.1029/2021TC006896.

ten Brink, U. S., Chaytor, J., Flores, C., Wei, Y., Detmer, S., Lucas, L., Andrews, B., and Georgiopoulou, A. Seafloor observations eliminate a landslide as the source of the 1918 Puerto Rico tsunami. *Bulletin of the Seismological Society of America*, 113(1):268–280, 2023. doi: 10.1785/0120220146.

Thompson Jobe, J., Briggs, R., Hughes, K., Joyce, J., Gold, R., Mahan, S., Gray, H., and Strickland, L. Datasets documenting neotectonic mapping of Puerto Rico. *U.S. Geological Survey Data Release*, 2024a. doi: 10.5066/P13KZZAZ.

Thompson Jobe, J., Briggs, R., ten Brink, U., Pratt, T., Hughes, K., Hatem, A., DuRoss, C., Reitman, N., Herrick, J., Nicovich, S., Collett, C., Scharer, K., and DeLong, S. Geologic Input Databases for the 2025 Puerto Rico—U.S. Virgin Islands National Seismic Hazard Model Update: Crustal Faults Component. *Seismological Research Letters*, page 1–27, 2024b. doi: 10.1785/0220230222.

Torres Angleró, K. H. Geologic deformation and faulting in the Ponce Limestone at the 877 northeastern end of the 2020 seismic sequence in Tallaboa – Guayanilla Bay Area. B.s. thesis, University of Puerto Rico Mayagüez, 2021.

Tuttle, M. Study of the source, magnitude, and recurrence time of large earthquakes affecting northern Puerto Rico, Final Technical Report. *U.S. Geological Survey NEHRP External*, page 37, 2006.

Tuttle, M. P., Dyer-Williams, K., Schweig, E. S., Prentice, C. S., Moya, J. C., and Tucker, K. B. Liquefaction induced by historic and prehistoric earthquakes in western Puerto Rico. In *Active Tectonics and Seismic Hazards of Puerto Rico, the Virgin Islands, and Offshore Areas*. Geological Society of America, 01 2005. doi: 10.1130/0-8137-2385-X.263.

U.S. Geological Survey. USGS one meter PR PRVI A 2018: U.S. Geological Survey. https://apps.nationalmap.gov/downloader/, 2020. Accessed: 2021-09-01.

U.S. Geological Survey. Quaternary fault and fold database for the United States, 2023. https://www.usgs.gov/programs/earthquake-hazards/faults.

U.S. Geological Survey, E. H. P. Advanced National Seismic System (ANSS) comprehensive catalog of earthquake events and products: Various. 2017.

Vičič, B., Momeni, S., Borghi, A., Lomax, A., and Aoudia, A. The 2019–2020 southwest Puerto Rico earthquake sequence: Seismicity and faulting. *Seismological Research Letters*, 93(2A): 533–543, 2022. doi: 10.1785/0220210113.

Vogt, P. R., Lowrie, A., Bracey, D. R., and Hey, R. *Subduction of aseismic oceanic ridges: Effects on shape, seismicity, and other characteristics of consuming plate boundaries*, volume 172. Geological Society of America, 1976. doi: 10.1130/spe172-p1.

Volckmann, R. Geologic map of the Cabo Rojo and Parguera Quadrangles, Puerto Rico, U.S. *Geological Survey Miscellaneous Investigations Map IMAP 1557*, scale 1:20,000, 1984. doi: 10.3133/i1557.

Weilert, L. and Laó-Dávila, D. A. Fault structure and segmentation of the Punta Montalva Fault in southwestern Puerto Rico using high-resolution digital elevation models. *Tectonophysics*, 860: 229921, Aug. 2023. doi: 10.1016/j.tecto.2023.229921.

Williams Associates. Geological evaluation studies for the Rio Valenciano Dam 1. Fault evaluation-Phase two, Appendix G in Luis O. Garcia Associates, Seismic hazard analysis, Rio Valenciano dam site, 2008.

Yoon, C. E., Cochran, E. S., Vanacore, E. A., Huerfano, V., Báez-Sánchez, G., Wilding, J. D., and Smith, J. A Detailed View of the 2020–2023 Southwestern Puerto Rico Seismic Sequence with Deep Learning. *Bulletin of the Seismological Society of America*, 113(6):2377–2415, 07 2023. doi: 10.1785/0120220229.

Zachariasen, J. and von Hillebrandt-Andrade, C. Holocene faulting of the Cerro Goden fault, Western Puerto Rico, Final Technical Report. *U.S Geological Survey. NEHRP External Grant Award Number QGR0082*, page 27, 2005.